Visual Hulls for Volume Estimation: A Fast Marching Cubes Based Approach

Phillip Simon Milne

A dissertation submitted to the Department of Electrical Engineering,
University of Cape Town, in fulfilment of the requirements
for the degree of Master of Science in Engineering.

Cape Town, February 2005

In memory of my grandfather

"*Owie*"
Owen Dudley Abrahams

1928–1994

Declaration

I declare that this dissertation is my own, unaided work. It is being submitted for the degree of Master of Science in Engineering in the University of Cape Town. It has not been submitted before for any degree or examination in any other university.

Signature of Author.....

Cape Town
21 February 2005

Abstract

This thesis describes a technique that can be used to compute and represent the visual hull of a 3D object. Silhouette-based methods rely on multiple views of an object to construct cone-like volumes that intersect, forming the visual hull. Multiple views can be generated using one of many different camera systems.

The visual hull is accurately calculated using high resolution voxel based models, which can be computationally expensive. The marching cubes algorithm improves upon the voxel based model by replacing surface voxels with polygonal patches, removing the sharp voxel corners characteristic of voxel based models. The positional accuracy of each surface patch is improved through the implementation of a binary search applied to all patch vertices.

Volume comparisons are made with ground truth measurements, computed at three different stages, in order to quantify performance and accuracy. The amount of computational time required is compared to the improvement in accuracy for each method.

The visual hull formed using the marching cubes algorithm on a low resolution voxel based model achieves better results in a shorter time than a high resolution voxel based model. The binary search is used to further improve the marching cube model and adds minimal computational expense.

Acknowledgements

I am grateful to the following for their contribution towards this thesis:

- Dr. Fred Nicolls, my supervisor, for his guidance.
- Prof. Gerhard de Jager, my co-supervisor.
- Keith Forbes for his advice and insight on the subject.
- Anthon Voigt for his enthusiasm and valuable reviews of my work.
- De Beers Technical, UCT and the NRF for their financial support.
- The members of the Digital Image Processing group for their contributions.
- Tarryn Kearns for the time spent proof reading.
- My parents, Merle and Leonard, and my sister, Sharon.
- My faithful friends, Meg and Emma.

Contents

List of Figures

List of Tables

Glossary

2D—Abbreviation of *two dimensional*. Has a coordinate system consisting of two orthogonal axes (x, y).

3D—Abbreviation of *three dimensional*. Has a coordinate system made up of three orthogonal axes (x, y, z).

Camera Calibration—The process that sets numerical values for the extrinsic and intrinsic parameters of a camera and/or the external 3D position and orientation of a camera frame relative to an external coordinate system [4].

Extrinsic camera parameters—External camera parameters. Describes the location and orientation of the camera with respect to the world coordinate system.

Intrinsic camera parameters—Internal camera parameters. Describes the total magnification of the imaging system resulting from both optics and image sampling as well as the principal point.

Grey-Scale Image—An intensity image. Pixels are represented by a single value that ranges from 0 (black) to 1 (white).

MATLAB—A high-performance programming language for technical computing.

MEX—Abbreviation of *MATLAB executable*.

Morphological Operators—Morphological operators are applied to binary images. They can be used to smooth or even extract edges. Basic operators include erosion, dilation, opening and closing.

Pixel—Abbreviation of *picture element*. It is the smallest element of a 2D image.

RGB Image—Abbreviation of *red, green and blue image*. Synonym for "colour image". Each pixel has separate values for red, green and blue.

RMS—Abbreviation of *root mean square*.

Segmentation—The process of separating an image into foreground (or target) and background regions.

Silhouette Image—An image that contains the silhouette of an object. Formed through the segmentation of a grey-scale or RGB image.

Topology—Branch of mathematics concerned with generalisation of concepts of continuity, limit etc.

Visual Cone—A cone-like volume that is formed by the projection of a silhouette from the camera centre.

Visual Hull—The closest approximation to an object that can be obtained with the volume intersection approach. The visual hull is the largest object that can be substituted for the actual object and still result in the same finite set of silhouettes.

Voxel—Abbreviation of *volume element*. A voxel is a cube.

Chapter 1

Introduction

The ability to accurately model real world objects in computer graphics and machine vision is an extremely powerful tool. Structural information contained in a 3D model is of great value in a wide range of systems: Computer games and animations often use objects from the real world; gesture recognition is simplified with a detailed knowledge of the shape of a person's limbs; shape classification systems require structural information of an object; geologists often require the size and shape distributions for a batch of rocks in various scientific evaluations.

Due to the demand from so many fields, a large amount of work has been done on modelling 3D objects. Previously, mostly offline systems were used. Optical systems, based on the acquisition of images that contain the object, can be separated into *active* and *passive* systems. Active systems, such as expensive laser scanners, cast a structured light over the object. Passive systems obtain information from the analysis of images that contain the object. Some passive systems are marker based, requiring undesirable invasive markers to be placed on an object. The silhouette-based approach has many advantages:

- It is relatively inexpensive.
- Cameras are easy to configure.
- It is non-invasive, as it does not require a marker system.
- Images contain both shape and texture information of a target object.

Structural information of an object is contained in any 2D image of that object. From a single view of an object, it is possible to make certain estimates about the dimensions of the object as well as its position relative to the camera. An estimate is improved with an increase in the

number of sufficiently different views available. The information from each camera needs to be coordinated so that precise 3D measurements can be inferred.

Over a number of years, many different methods for representing 3D models have been developed, some more efficient than others. The *visual hull* of an object is generally accepted as an adequate representation[14] and hence, the volume of the visual hull is a good approximation to the actual volume of the object.

Voxel-based methods use a number of small cubes (or 3D pixels) to construct the visual hull. Although the resultant models are extremely accurate at higher resolutions, they are computationally expensive. The surface of a voxel-based model is made up of a number of cubes, causing the model's surface to appear jagged. A representation consisting of polygons would provide smoother and easier to manipulate visual hull models.

One solution to this problem is to build a coarse voxel model and then apply an algorithm known as *marching cubes*, which replaces surface cubes with polygons. With minimal effect on the computational time required, this algorithm can drastically improve the accuracy of the model.

1.1 Objectives of this Thesis

Many systems use the volume distribution of rock samples as an input to control a process. Manual volume measurements for a large set of rocks are tedious. Computing the volume from the visual hull of a rock is a fast and automated process.

The objective of this thesis is to implement a system that can quickly compute the volume of an object from its visual hull using multiple views of the object. A target object's visual hull will be calculated from silhouette images, obtained in an accurately calibrated camera system. The visual hull will be described in three stages:

- **Voxel Based Models** - A 3D space is partitioned into cubic volume elements (or *voxels*) and a binary marking system is used to represent the visual hull's basic structure.
- **Marching Cube Models** - The marching cubes algorithm assigns triangular patches to surface voxels of the voxel-based visual hull.
- **Modified Marching Cube Models** - The positional accuracy of each triangle corner created with the marching cubes algorithm is improved by applying a binary search.

The system's performance will be quantified at the three stages of the algorithm by comparing

the amount of time required to complete the visual hull computation and the RMS percentage volume errors.

1.2 Thesis Outline

This thesis discusses the theory needed to build the visual hull of an object using silhouette projection methods for volume estimation. An algorithm is developed and tested at three stages on a data set of stones. The following is a brief summary of the remaining chapters.

Chapter 2 contains a literature review that gives a background to the theoretical ideas involved in the implementation of this project. Valuable sources of information on camera geometry and methods used for volume computation are summarised. Practical applications for automated volume estimators are examined and work done in the field of "shape from silhouettes" is contained in this chapter. Various methods for representing the visual hull of an object are introduced.

Chapter 3 describes the camera system used to obtain images, as well as the way that 3D measurements are obtained from 2D images. The pinhole camera model is described and the three coordinate systems that it defines are listed. Various environments that accommodate for the capture of multiple views of an object are investigated.

Chapter 4 discusses the concept of "volume intersection", which is used to obtain the visual hull of an object from an accurately calibrated camera environment. The segmentation of images and the projection of silhouettes into a 3D space are also covered.

Chapter 5 describes the ideas associated with voxel-based visual hulls. A volume is partitioned into small cubic cells and each cell's value is set so that the volume represents the visual hull of an object. This chapter makes use of 2D analogies to explain some of the key ideas.

In chapter 6, the marching cubes algorithm is explained. The marching cubes algorithm approximates the intersection of a surface through a cube by tiling it with triangular patches. 2D analogies are used to illustrate the effects of the algorithm.

An extension to the marching cubes algorithm is introduced in chapter 7. The extension applies single iterations of a binary search to the vertices of each surface patch, resulting in a better visual hull approximation of the object. A 2D analogy of this algorithm simplifies its description.

Details on the algorithms used to implement the voxel-based, marching cubes and binary search visual hulls are provided in chapter 8. An accurately calibrated camera system captures multiple views of a target object. Captured images are segmented to form silhouettes that are extruded

and used to compute the visual hull model using voxel-based methods. The marching cubes algorithm is applied to the voxel model, replacing surface voxels with triangular patches. This has the effect of smoothing the visual hull surface. A binary search is used to further refine the accuracy of the visual hull. Techniques that are used to compute the volume of voxel based and marching cube models are described in this chapter.

Chapter 9 presents the testing methods and discusses the results obtained from these tests. This chapter contains a performance comparison between the three stages of the algorithm. A data set of stones that represent a wide distribution of naturally occurring shapes is used to test the viability of the system. Accuracy and speed improvements resulting from the voxel model and the marching cubes algorithm, both with and without the binary search, are be evaluated. A method's accuracy is measured using RMS percentage error statistics, which are computed through a comparison of computed visual hull volumes with ground truth values. The increase or decrease in processing time required is also studied.

Finally, chapter 10 presents conclusions, limitations and proposes scope for future research. The link to a website containing a tutorial on the algorithms, as well as working code, is also provided.

Chapter 2

Literature Review

This chapter provides a description of work already done in the various fields discussed in later chapters. Each source of information contains valuable insight on ideas and concepts, which results in the implementation of a working algorithm that can accurately and quickly compute the volume of an object from multiple image views.

Volume estimation systems are outlined in section 2.1. The sections that follow briefly describe work already done on the subject of visual hull reconstructions. Section 2.3 looks at the methods used to compute the volume of a visual hull.

2.1 Background

The size and shape distribution for a batch of stones has a major role to play in the strength, stability and performance of concrete and asphalt. Manual systems use sampling techniques to monitor the distribution of particles. This method is time consuming and makes real-time feedback for control purposes impossible.

A 3D-laser scanning technique is used by Lanaro *et al.* [11] to evaluate coarse-grain aggregate-particle images. They are able to achieve reliable results for both the shape and topographical parameters of particles. The laser sensor used in experiments is sensitive to environmental conditions, making it more suited to laboratory investigations.

2D images are used by Bantaa *et al.* [12] to determine the distribution of particle sizes in asphalt pavements. They estimate the size and shape characteristics of multiple stones from a single segmented view. The single view means that stereo information is not available and therefore, an average value for height is used when computing particle volumes. In their system, exact

volume measurements for a single particle are not critical. Rao *et al.* [28] use three camera views, which provide them access to vital stereo information. Particles are individually sent through their system, providing better estimates at slower speeds. Cameras are positioned in a way that allows them to capture orthogonal views of a particle, resulting in the calculation of more accurate volume estimations. Their system is used to automate the determination of flat and elongated particles, angularity, and gradation.

2.2 Shape from Silhouette

In many applications it is intrusive or impractical to attach foreign marker objects to the body of the subject. Non-intrusive techniques are therefore more desirable.

A human observer can, in most cases, recognise an object from the shape of its silhouette. The silhouette of a 3D object is therefore a valid source of shape information. The concept of using silhouettes for 3D shape reconstruction was first introduced by Baumgart in 1974. In Baumgart's PhD thesis [3], four silhouette images are used to estimate the 3D shape of a baby doll and a toy horse. Silhouette images are the result of segmenting a grey-scale or RGB image into *target* and *background* regions. Segmentation is a widely researched branch of image processing and is available in many forms, such as region growing, contour modelling and thresholding.

Hamblin *et al.* [10] show that there is a relationship between the complexity of a particle and the sensitivity to the positioning of viewing points. The more uniformly a particle's dimensions vary through different planes, the less a viewing technique affects its approximations.

Olsson *et al.* [26] uses a single stationery camera to capture views about a rotating object. The use of a single camera, instead of multiple cameras, makes their method more cost effective, while the rotating object enables them to retain the ability to capture multiple views.

Pollefeys [27] presents a technique that can obtain realistic 3D models of existing monuments from a few old photographs. The flexibility of his technique allows it to be used on video material. His algorithm is minimally dependant on calibration information and therefore, produces scale invariant models.

2.2.1 Camera Geometry

Camera calibration is a widely studied research topic in computer vision. Before computer vision, it was extensively investigated in the field of photogrammetry. Calibration is a necessary

step in inferring 3D measurements from 2D images [19].

Chavarriaga *et al.* [4] provides an in-depth description of the camera model, as well as valuable mathematical detail on the calibration process.

Various methods have been developed to determine the pose corresponding to each camera in a multi-camera system. Tsai [33] has developed an autonomous technique for camera calibration using standard off-the-shelf cameras. Tsai's method uses an advanced bar coded pattern printed on a calibration object. The calibration object is required to be a fixed distance from the camera.

2.2.2 The Visual Hull

The term *visual hull* was formally defined in 1991 by Laurentini [13]. For more than a decade before this, it had been used in a general sense by researchers. Laurentini defines the visual hull as the entity used to describe the largest object consistent with *all possible* silhouettes. However, the term is usually used to refer to the largest object that is consistent with a *finite set of available* silhouettes. The visual hull is known to include the object and to be included in the object's convex hull [14].

Shakhnarovich *et al.* [29] describes a system that uses four, evenly spaced, fixed cameras at approximately the same height. Using visual hull reconstructions, they are able to recognise a person from a combination of facial features and gait.

Cheung [6] uses a single camera to capture multiple view silhouettes of a moving subject. Using a model of the human body, a coarse visual hull of the subjects is initially computed. As time progressed, and more silhouette information became available, the accuracy of the visual hull model improves.

Niem *et al.* [25] use a single camera and a turntable to obtain multiple silhouette images of an object at different viewpoints. The relative poses of the turntable platform with respect to the camera are determined with the aid of a calibration object. They computed the visual hull model with volume carving techniques and generated a triangular mesh to represent its surface.

A newer method, implemented by Matusik *et al.* [21] makes use of polygons to represent the visual hull. They developed an algorithm that reduces 3D intersections to simpler 2D intersections. Their algorithm produces view-independent representations that are computed very quickly. The visual hull is formed by its polygonal faces, each of which lie on a face of one of the visual cones. The visual hull faces are therefore formed by the intersection of the faces of each visual cone with all remaining visual cones.

2.2.3 Voxels and the Octree Model

Volume intersection techniques for constructing a volumetric description of an object from multiple views, was first proposed in 1983 by Martin and Aggarwal [20]. Ahuja and Veenstra [1] presented an extension to this technique, which generated an octree to represent an object from any subset of 13 standard viewing directions.

The main thrust of Small's MSc thesis [30] is to be able to compute the visual hull in real-time. Binary volumetric images are used to represent the visual hull model. Small's review of calibration techniques and volume intersection gives useful insight on the subjects.

2.2.4 Marching Cubes

In 1987, Lorensen and Cline [18] present an algorithm that creates a triangular mesh for medical data. Known as "marching cubes" due to the way it "marches" from one element to the next, the algorithm is considered to be the basic method for surface rendering in medical applications. In this text their original algorithm will be referred to as MC15. They use MC15 to process 2D computer tomography slices in scan line order, while maintaining inter-slice connectivity. A lookup table, containing 15 possible surface intersections allows the MC15 algorithm to be fast. MC15 can be applied in other areas, as for example, in the visualisation of implicitly specified functions or even the visualisation of calculation results. They also note that the generated surface contains a large number of triangles.

Nielson *et al.* [24] found that MC15 has no topological guarantees for consistency and produces visual hull surfaces containing small holes or cracks due to certain voxel face ambiguities. Using definitions of *separated* and *non-separated* voxel vertices, they are able to propose a modification to MC15 that implements face tests to resolve the ambiguities. They do not guarantee the correct topology either, and propose an internal test to resolve other ambiguities. In 1995, Chernyaev [5] showed that there are 33 topologically different surface intersections and not 15. His algorithm will be referred to as MC33. Chernyaev found ambiguous cases that are not visibly obvious and uses the suggested internal tests to resolve the remaining ambiguous voxel arrangements.

Montani *et al.* [23] noted the topological inconsistency, computational efficiency and excessive data fragmentation as disadvantages of MC15. They propose a method to minimise the number of triangular patches specified in the marching cubes surface lookup table, reducing the amount of data output and improving the computational efficiency. The test table which they use to resolve ambiguous voxel configurations is shown in figure A.1 of the appendices.

In a paper by Lewiner *et al.* [16], an efficient and robust implementation of Chernyaev's MC33

algorithm is described. Detailed information, covering lookup tables, voxel labelling systems and tests to resolve voxel ambiguities, is provided. Their system guarantees a consistent surface without holes or cracks.

Tarini *et al.* [31] developed a fast and efficient version of the marching cubes algorithm, called *marching intersections*, to implement a volumetric based visual hull extraction technique. Using a large 3D mesh configuration, scans of the target are made. The point at which the ray intersects with the target is stored. The paper also provides a good definition of the visual hull computed from images captured with a turntable.

In Wong's PhD thesis [34], a detailed description of the entire visual hull computation process can be found. Wong describes the static properties of silhouettes and then studies the dynamic properties of a moving camera system. He uses an octree system to represent the visual hull, and then applies the marching cubes algorithm, which allows the constructed 3D model to be displayed efficiently in conventional graphics rendering systems.

2.3 Visual Hull Volumes

Part of the objective of this thesis is to compute the volume for a given visual hull. To compute the volume of an voxel based model is as simple as summing the volume of a list of cubes. The volume enclosed by a polygon model can be calculated in a number of ways. The method used is summarised in section 2.3.1. It was not necessary to find alternate volume computation techniques as this method was deemed adequate.

2.3.1 Volume Computation for Polyhedra

A marching cube surface consists of a list of polygonal surfaces, that are stitched together to form the visual hull of an object. Many methods for calculating the volume, mass or moment of inertia of polyhedra are computationally expensive or produce approximate results. Lien and Kajiya [17] developed a technique that not only produces an exact solution, but is also efficient. They integrate a set of tetrahedra formed by each triangular face and the origin. Their method also allows for the computation of the visual hull's centroid.

Chapter 3

Camera System

When taking 3D measurements from 2D images, knowledge of the intrinsic and extrinsic parameters of the camera is crucial. In a multi-camera environment, the relative poses and positioning of each camera is also of great importance. This criteria requires that the camera system involved be accurately calibrated. A number of environments that enable the capture of multiple views of an object are also introduced in this chapter.

3.1 Calibration Process

Calibration is the process that enables the setting of numerical values for the geometrical and optical (intrinsic and extrinsic) parameters of the camera and/or the external 3D position and orientation of the camera frame relative to an external coordinate system [4]. The output of this process is normally a pose transformation matrix, which is a 4×4 matrix that applies a *rigid body transform* to a set of points. A rigid body transform performs a rotation and a translation on a set of points, while preserving the lengths and angles between the points.

System calibration can be done in many ways. One of the more commonly used methods involves the use of a calibration object. Once calibrated, each camera is associated with a *pose transformation matrix* that enables a transformation from the camera's own reference frame to a world coordinate system that encompasses the entire system [9].

A calibration object can be of any size or proportion (preferably matched to the camera's field of view), as long as its dimensions are accurately known. An example of a 20-sided calibration object is shown in Figure 3.1. This object was constructed from cardboard. Each of the triangular faces is marked with a binary labelling system. Using an object of this type enables an

uncalibrated system to calculate the exact orientation of the object with respect to each camera's reference frame. Once all of these orientations have been computed, each camera's pose and position in the system can be calculated [8].

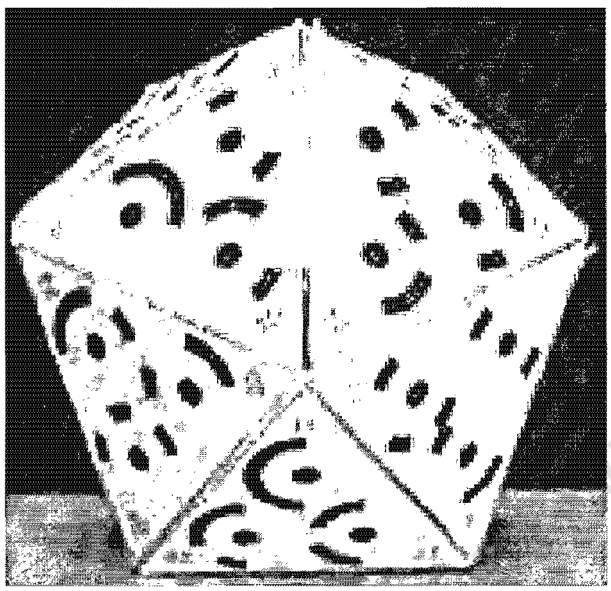

Figure 3.1: The 20 faced calibration object constructed from cardboard. Each face is marked with a unique binary coded pattern.

Most cameras perform a perspective transformation on points in a 3D space to 2D points in the retinal (or image) plane. The geometry of 2D images was first studied by Italian artists during the Renaissance so that they could reproduce objects from the real world more accurately [7]. Although real cameras have apertures of finite size and use lenses for focussing light onto the retinal plane, *the pinhole camera model* is an excellent approximation of the imaging process [9].

3.1.1 Pinhole Camera Model

This perspective projection model, illustrated in Figure 3.2, assumes that light enters the camera through a dimensionless point (or pinhole) at the camera centre and projects onto the retinal plane.

The camera centre, also called the *focal point*, is situated between the object and retinal plane. The imaged object appears inverted in the retinal plane due to light rays travelling through the optical centre and onto the retinal plane. Positioning the retinal plane in front of the camera, as in Figure 3.2 (b), is geometrically equivalent and sometimes seen as being more intuitive [32].

The pinhole camera model defines an *image coordinate system* and a *camera coordinate system*. In a multi-camera system, a *world coordinate system* is also defined so that camera positions are

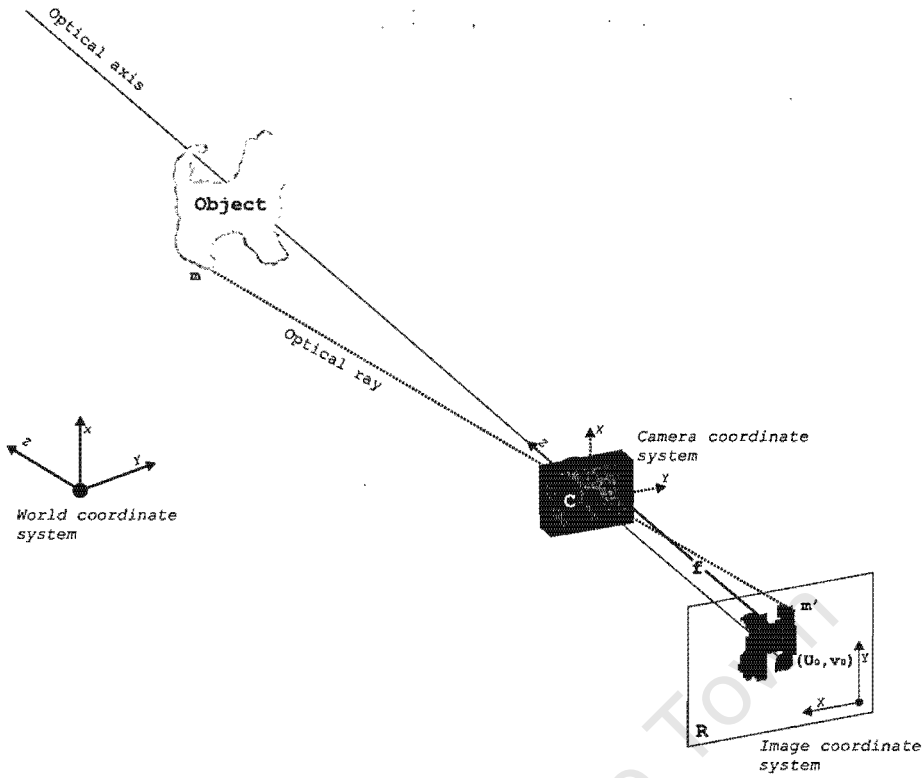

(a)

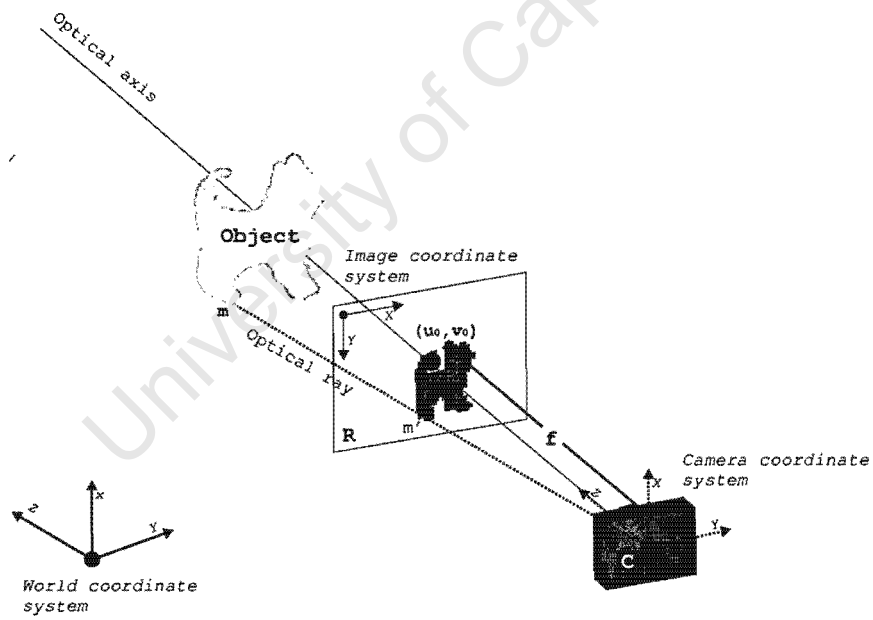

(b)

Figure 3.2: In the pinhole camera model, the retinal plane ($\Re$) and the camera centre (a point C that does not belong to $\Re$) are shown. C is the focal point. The distance from the focal point to the centre of the retinal plane is the focal length, f. The scene point, m, on an object, is mapped to the point m' in the retinal plane. A right-handed coordinate system is employed. The imaged object is inverted in illustration (a). The model in (a) is geometrically equivalent to the model shown in (b), where the retinal plane is situated between the camera centre and the imaged object.

known relative to each other.

Affine Image Coordinate System

Most images use pixels as their unit of measurement, but this is dependent on the technology of the camera. Images use a 2D coordinate system that generally has its origin positioned in the top left corner of the image. The point that is directly in front of the camera, situated in the retinal plane, is known as the principal point and has coordinates (u_0, v_0). This point is near the centre of the image.

Euclidean Camera Coordinate System

In the camera's 3D coordinate system, the camera is positioned at the optical centre (0,0,0). The focal length (f) is the distance from the optical centre along the optical axis to the point of intersection with the retinal plane. This point of intersection, known as the principal point (which is near the image centre), is situated at $(0,0,f)$. Camera coordinates are generally measured in metres or millimetres.

World Coordinate System

The world coordinate system is introduced to link together all the camera systems available. It is used to describe the location and orientation of each camera with respect to the others.

Retinal Plane to Camera Reference Frame

To map a point in the retinal plane to a point in camera coordinates, the units need to be converted to match that of the cameras. The retinal plane is a distance f from the optical centre, making the z coordinate of any point in the image equal to f. The x and y coordinates of the image need to be translated by u_0 and v_0 respectively, as the principal point in image coordinates is at (u_0, v_0) and $(0,0,f)$ in the camera's coordinate system.

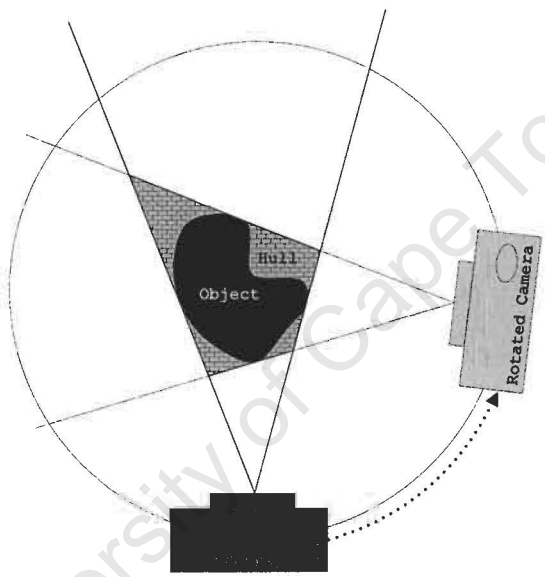

Figure 3.5: A single camera is used to view a black *target* object. The camera is rotated around the object to obtain two views. The textured grey section represents the resultant hull.

3.2 Multi-view Camera Systems

Multiple image views can be obtained from a variety of different camera systems. The visual hull becomes a closer approximation of the object with an increase in the number of significantly different available views. Three different camera arrangements for generating multiple views of an object follow. Optimum positioning of the cameras is a subject that is not covered.

3.2.1 Multiple Camera Environment

Multiple cameras are arranged about the object. A multi-camera arrangement is the most intuitive as well as the simplest of the three to implement. Due to the use of more cameras, it is also the most expensive. Figure 3.3 shows a 2D illustration of this type of camera arrangement using only two cameras. Since the intrinsic parameters of each camera may vary, each camera has to be separately calibrated.

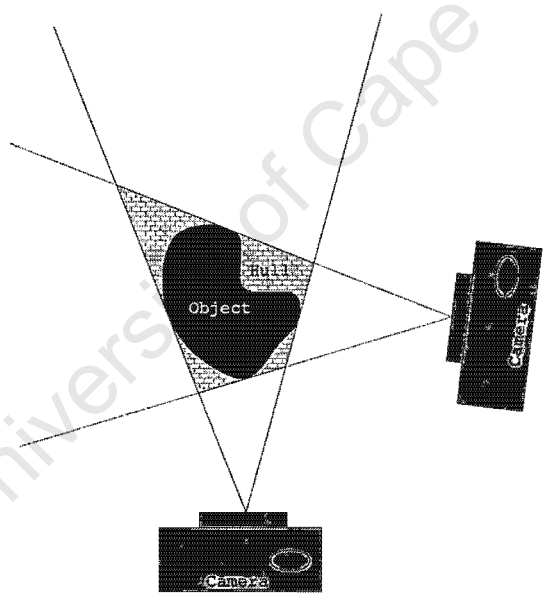

Figure 3.3: Two cameras are used to view a black *target* object. The textured grey section represents the resultant hull.

3.2.2 Mirror and Camera Environment

Mirrors can be used to reduce the number of expensive cameras required in the implementation. Multiple views of the object are provided by mirrored reflections of the object (see Figure 3.4). This increases the mathematical complexity of the system. An advantage of this arrangement is

that the addition of extra mirrors, rather than expensive cameras, makes more views of the object available. A possible negative aspect is that the use of mirrors results in a decrease in clarity of the reflected object due to the object appearing smaller in the reflected camera view than the direct camera view.

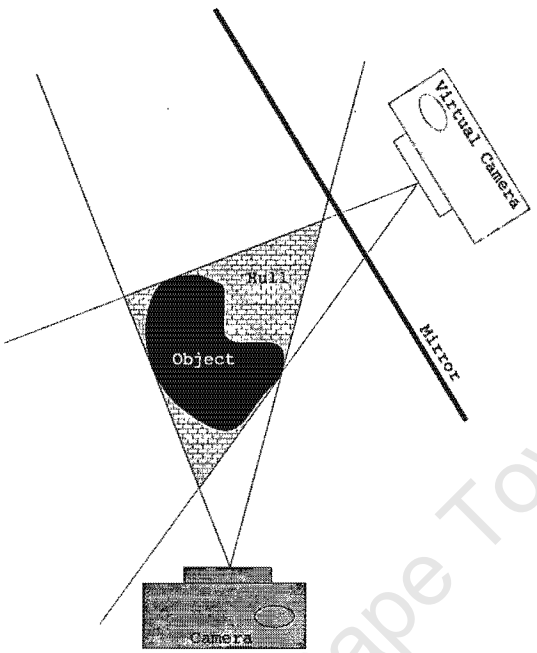

Figure 3.4: A single camera is used to view a black *target* object. The mirror reflects the image of the object creating a view from a virtual camera. The textured grey section represents the resultant hull.

3.2.3 Rotating Camera or Object

Multiple views of an object can be obtained by rotating it with respect to the camera and capturing images in sequence. A rotational system is not always practical in a real time environment, but is ideal for offline situations. The simplest method involves placing an object on a rotating platform that allows controlled increments through 360°. The accuracy of this system is dependent on the number of rotational increments that the platform moves through, as well as the elevation of the camera relative to the rotating platform. This system is equivalent to rotating a camera about a stationary object as shown in Figure 3.5.

Chapter 4

The Visual Hull

Laurentini defines the visual hull of a 3D object as being "the closest approximation of S [an object] that can be obtained with the volume intersection approach" [13]. The visual hull is the largest volume that can be substituted for the actual object and still result in the same finite set of silhouettes. Significant concavities, such as the inside of a tea cup, are not captured in visual hull representations of an object.

The visual hull can be an exact copy of the object. It is never smaller than the object as it always completely encloses the object. Compared to the convex hull, the visual hull is a closer representation of a 3D object's structure. Due to the visual hull being computed from an object's silhouette views, its shape is dependant on the shape of the object combined with the region of the object viewed in the silhouettes.

This chapter begins with a description of the method used to compute an objects silhouette given an image of the object. In the section that follows, volume intersection is investigated.

4.1 Silhouette Extraction

Identifying and reconstructing 3D objects based on 2D images has been under investigation for a number of years. Even though silhouette-based approaches neglect surface features that could be used to identify the object, they are still an excellent tool for object recognition.

The silhouette of any 2D image can be obtained through a process known as image segmentation. This process is one of the most fundamental and important components in image processing. The quality of an application is generally dependent on the accuracy of segmentation used, and hence a good segmentation algorithm is extremely important [22]. Segmentation involves decomposing

an image into parts that are meaningful with respect to a particular application. In the visual hull construction application, image regions are classified into the following two categories:

- *Foreground* (or Target)
- *Background*

Figure 4.1 shows the segmentation of a grey-scale image of a small plastic cat into *foreground* and *background* regions. A silhouette image's pixels have binary colour values that can be either 1 or 0, which indicate the pixel's region classification.

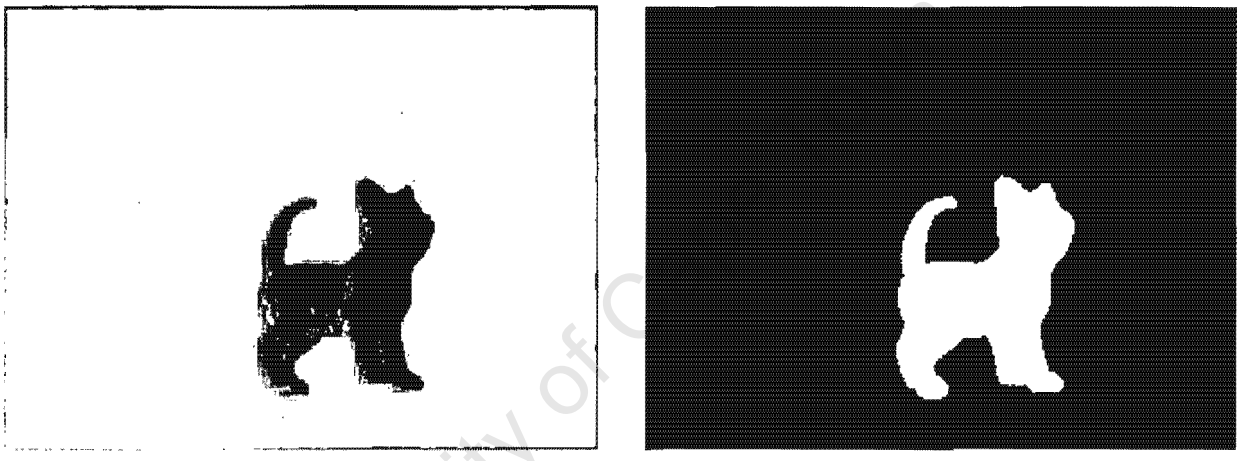

(a) Grey-Scale Image (b) Segmented Image

Figure 4.1: The grey-scale image of a small plastic cat is shown in (a) and its associated silhouette image in (b). Image (b) has been segmented into white *foreground* and black *background* regions.

There are a wide variety of segmentation algorithms available. Region growing, watersheds and contour modelling [2] are among a few of the more intelligent algorithms that have been developed. A less complex method places a simple threshold on an image's intensity values.

Two dimensional images are made up of a number of small square picture elements called *pixels*. In grey-scale images, pixels store an intensity value that ranges between 0 and 255 or 0 and 1. The threshold must lie within this range. Intensity values exceeding the threshold are classified as *foreground*, while values below the threshold are classified as *background*. Figure 4.2 illustrates the concept of threshold segmentation. Using a threshold on an image provides adequate results and also requires the least amount of processing time. It was for these reasons that thresholding was used as the preferred segmentation technique.

13	15	14	13	13
14	55	56	13	13
15	14	55	57	13
15	55	58	57	14
14	13	13	13	14

(a)

0	0	0	0	0
0	1	1	0	0
0	0	1	1	0
0	1	1	1	0
0	0	0	0	0

(b)

Figure 4.2: This figure shows a grid of intensity values. In the first grid, a threshold of 50 has been applied, and highlighted in white. The second grid shows how each value is labelled as *foreground* (marked with ones) and *background* (marked with zeros).

Threshold segmentation, although relatively fast compared to other segmentation algorithms, can result in grainy disconnected targets. Generally, better segmentation results are obtained through the selection of an appropriate background, combined with controlled lighting. Morphological operators are able to smooth out the grainy appearance of a target and improve the segmented output.

4.2 Volume Intersection

Volume intersection, used in Laurentini's definition of the visual hull, is described here. First, computing the position of a 3D point is investigated, after which the idea is expanded to accommodate the intersection of a number of volume's that form the visual hull.

4.2.1 Estimating the Position of a Point

Using a single image (i), the 3D position of a point (M_{xyz}) is constrained to lie somewhere along the line projected from the camera centre (C_0^i) through the imaged point (M^i) to infinity. The equation of the line is given in equation 4.1.

$$M_{xyz} = C_0^i + S * (M^i - C_0^i) \tag{4.1}$$

The variable S is an unknown scaling factor relating to the depth of the point. This value can only be computed with the addition of a second view of the point, captured from a different location. The point must lie at the intersection of the lines projected from each camera. However, due to various inaccuracies inherent of the system, projected lines are not guaranteed to intersect. For this reason the point is assumed to be positioned so that the perpendicular distance to each projected line is minimised. Using equation 4.2, we can solve for S.

$$b = \begin{bmatrix} C_x^1 - C_x^2 \\ C_y^1 - C_y^2 \\ C_z^1 - C_z^2 \end{bmatrix} \tag{4.2a}$$

$$A = \begin{bmatrix} M_x^1 - C_x^1 & M_x^2 - C_x^2 \\ M_y^1 - C_y^1 & M_y^2 - C_y^2 \\ M_z^1 - C_z^1 & M_z^2 - C_z^2 \end{bmatrix} \tag{4.2b}$$

$$S = A \setminus b \tag{4.2c}$$

Substituting this value into equation 4.1 gives us the 3D coordinates of M_{xyz}.

4.2.2 Visual Cone Projection

By the same principle used in the previous section, an object must lie within the cone-like volume that is formed by an extrusion of its silhouette. A silhouette is extruded by projecting each point in the silhouette from the camera centre through its location in the retinal plane. The volume formed is known as a *visual cone* and it completely encloses the object (see Figure 4.3).

With the addition of a different silhouette view of the object, the visual hull becomes a closer representation of the object's shape and location. Figure 4.4 shows two visual cones that intersect to form the visual hull of an object. As the number of available views increases, so the accuracy of the model improves. Figure 4.5 shows the effect that an increasing number of views has on the visual hull.

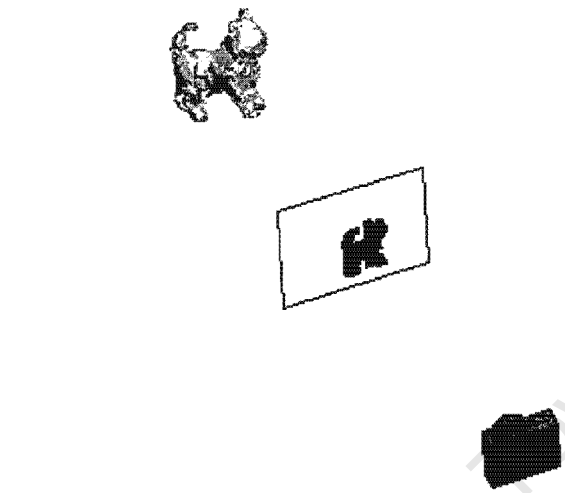

(a)

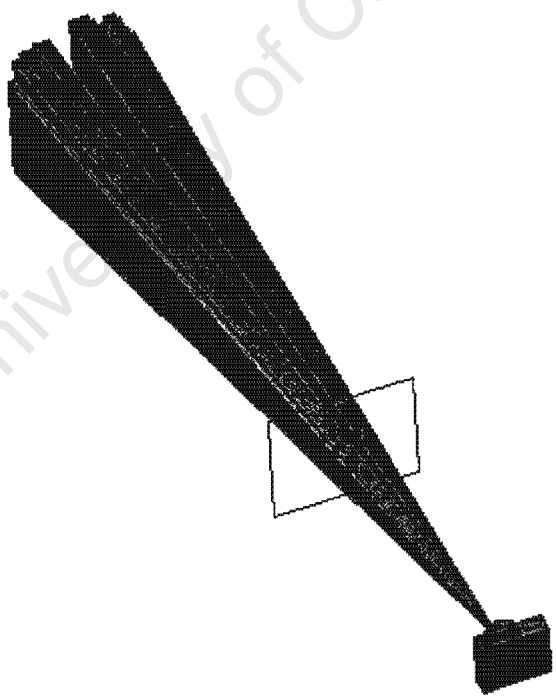

(b)

Figure 4.3: The visual cone of a silhouette is projected from a camera centre. The silhouette image that is seen by the camera is shown in image (a). Image (b) shows the projected visual cone that encloses the object.

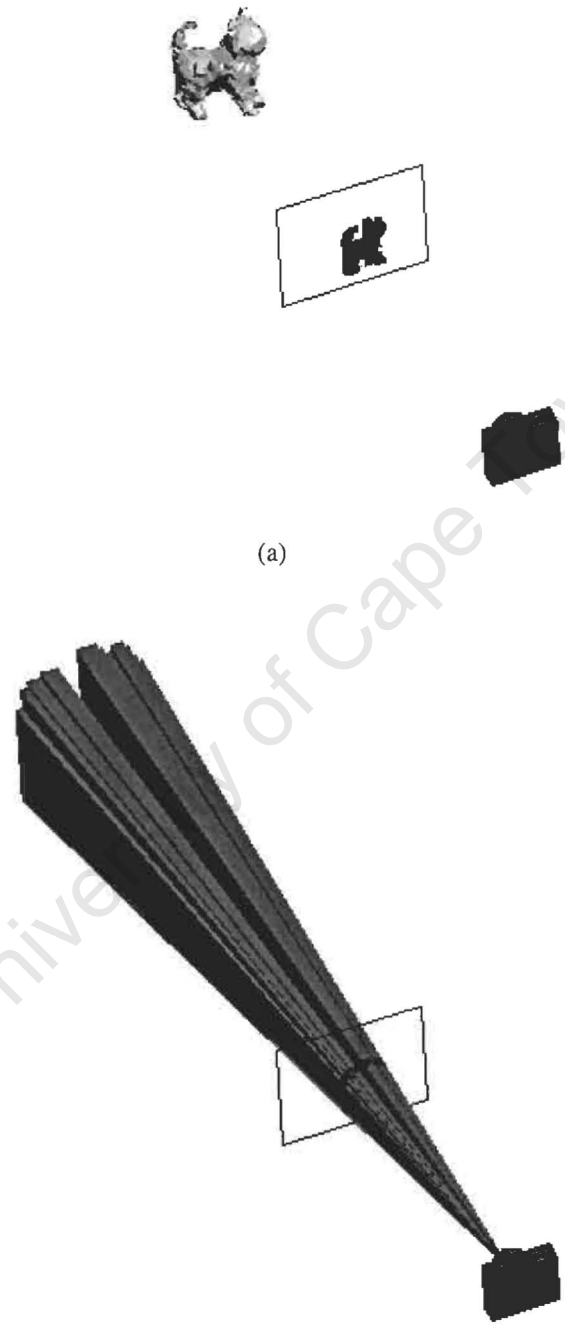

(a)

(b)

Figure 4.3: The visual cone of a silhouette is projected from a camera centre. The silhouette image that is seen by the camera is shown in image (a). Image (b) shows the projected visual cone that encloses the object.

(a) 2 Views

(b) 3 Views

(c) 4 Views

(d) 5 Views

Figure 4.5: As the number of available silhouette views increases, the visual hull becomes a closer representation of the object. The number of views used to generate each of the visual hull models is shown below the model.

Chapter 5

Voxel Based Visual Hull Models

In the first section of this chapter, a voxel and its characteristics are described. The section that follows details the way in which voxels can be used to represent the visual hull. The method used to compute whether or not a voxel projects to inside or outside the target is then introduced. Lastly, the data structure used to store the volume data is discussed.

5.1 The Voxel Concept

The voxel concept is more easily explained using a 2D analogy. In Figure 5.1, the 2D image of a cat is iteratively subdivided 3 times into 32 square cells. Any cell that has a corner which is overlapped by the cat is marked as *full*. Every other cell is part of the *empty*. The combination of all *full* cells results in a coarse 2D visual hull of the cat.

By expanding to 3D, the idea of dissecting a 2D image into square cells and marking each cell as *full* or *empty*, it is possible to represent the 3D visual hull of a target. A volume in space is dissected into equal sized cubic volume elements (known as *voxels*) using three orthogonal sets of parallel planes, forming a spacial occupancy map known as a *cuberille grid*[24]. A cuberille grid's 2D equivalent is a mesh made up of squares as seen in Figure 5.2). Each voxel is associated with a binary value that indicates whether the voxel is part of the target or part of the background.

5.1.1 Properties of a Voxel

Voxels in a 3D cuberille space are analogous to pixels in a 2D image. They represent cubic volumes of space. A single voxel can be described as a scaled cube in a 3D coordinate system.

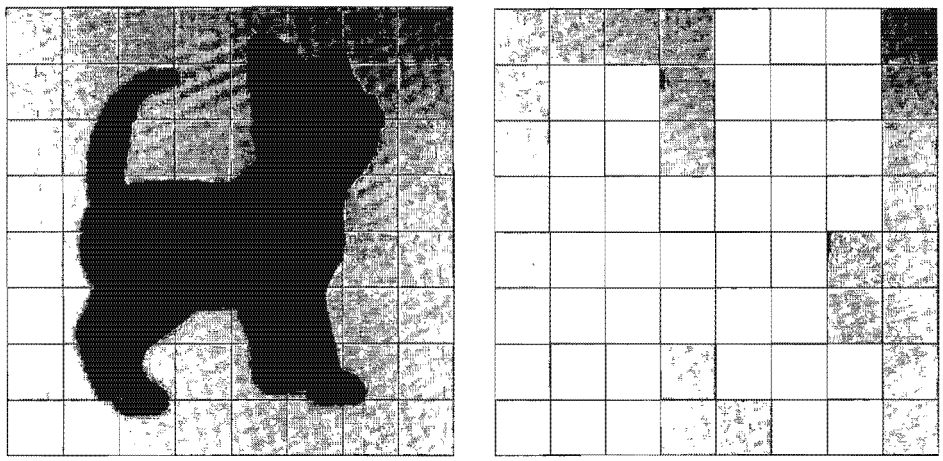

(a) (b)

Figure 5.1: In this illustration, the image of a cat is shown in a. The squares in 2D correspond to voxels in 3D and the 2D target object is equivalent to the actual 3D visual hull. Both images have been iteratively divided 3 times into 32 square cells (2D voxelisation). Cells categorised as *full* contain a while fill, while *empty* cells are left unchanged.

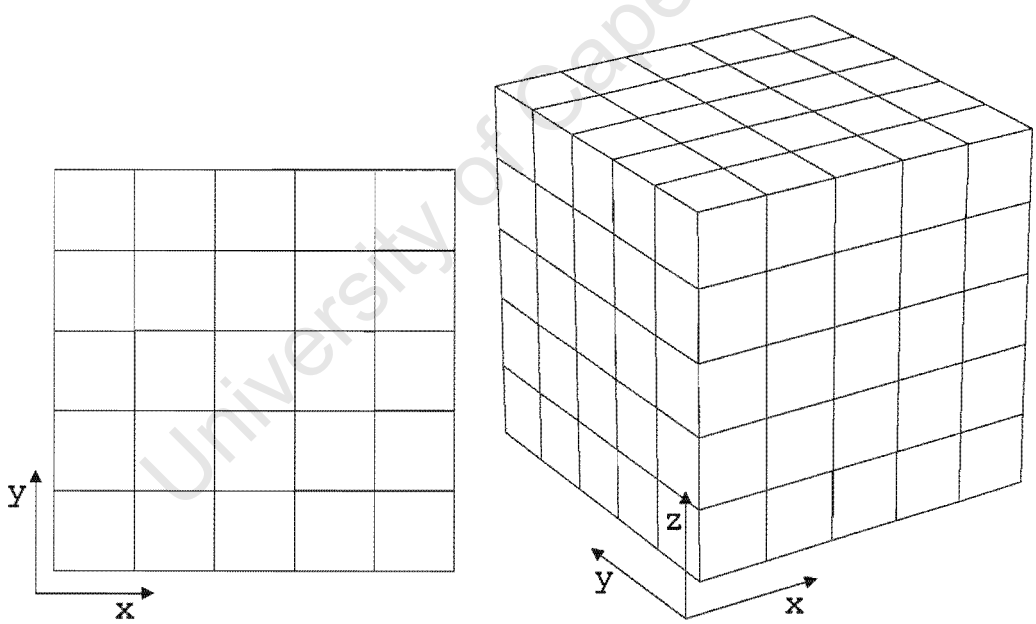

(a) 2D Grid (b) 3D Cuberille Grid

Figure 5.2: The 2D grid of an image is equivalent to the 3D cuberille grid used for a voxel-based visual hull model.

A voxel is defined by the 3D position of its centre and the length of one of its sides. Voxels differ slightly from pixels in that their eight vertices are ordered (as shown in Figure 5.3) and can each be assigned a different binary value. These assigned vertex values decide the voxel's value or

occupancy category. A voxel can fall into one of three occupancy categories:

- **Full** : The voxel is *completely inside* the visual hull.
- **Partial** : The voxel is *partially inside* the visual hull.
- **Empty** : The voxel is *completely outside* the visual hull.

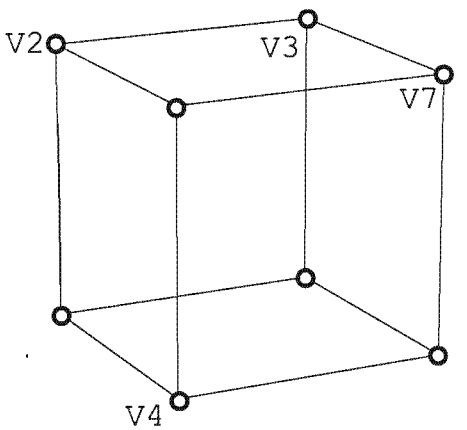

Index = | V0 | V1 | V2 | V3 | V4 | V5 | V6 | V7 |

Figure 5.3: The eight-bit indexing system used to indicate the occupancy of the eight corners of a cube. If the corresponding corner is occupied, a bit is set to 1. A bit is set to 0 if the corner is empty.

5.1.2 Voxel Occupancy Computation

Points inside a cuberille space can be either *part of the target* or *part of the background*. Each point that is situated inside a silhouette's visual cone, when projected into the retinal plane, will be contained inside the image of the object. In a single camera system, all of these points would make up the target object's visual hull. By constraining the visual hull with more views of the target, the number of points that are part of the visual hull decreases. In multiple camera systems, a point can lie within the visual cone of one silhouette and be outside the visual cone of another. This point is then not part of the visual hull. If a point projects to background in any one of the views available, it is *not* part of the target, and must be declared *empty*. For a point to be part of the visual hull, it must project to being inside the image of the object in the retinal plane for all available camera views.

The projection and testing of every single point that lies inside a visual cone is impractical. Instead, an enclosing space is divided into voxels and all points inside a voxel are placed in the same category.

A voxel's occupancy is computed by projecting each of its eight vertices into all of the silhouette images of the target. If a projected voxel vertex is found to be inside the target in *all* of the silhouettes, it must be part of the target. A vertex that projects to outside the target in *any* silhouette is part of the background. Once all the vertices have been tested, assumptions are made so that the occupancy category of the voxel can be decided[1].

- If *all eight* vertices are part of the target, the voxel is assumed to be *full*.
- If some, but *not all* vertices are set as target, the voxel is assumed to be on the surface of the visual hull. These voxels are uniformly categorised as *partial*.
- If *none* of the vertices are part of the target, the voxel assumed to be *empty*.

Figure 5.4 illustrates how the different voxel occupancy categories are computed. There are situations where these assumptions cause inaccuracies. Figure 5.5 shows how a voxel can have part of the object passing through it, and yet still be incorrectly classified as empty. Targets that contain snake-like or sharply peaked edges result in voxels being incorrectly categorised and hence creates an inconsistent visual hull.

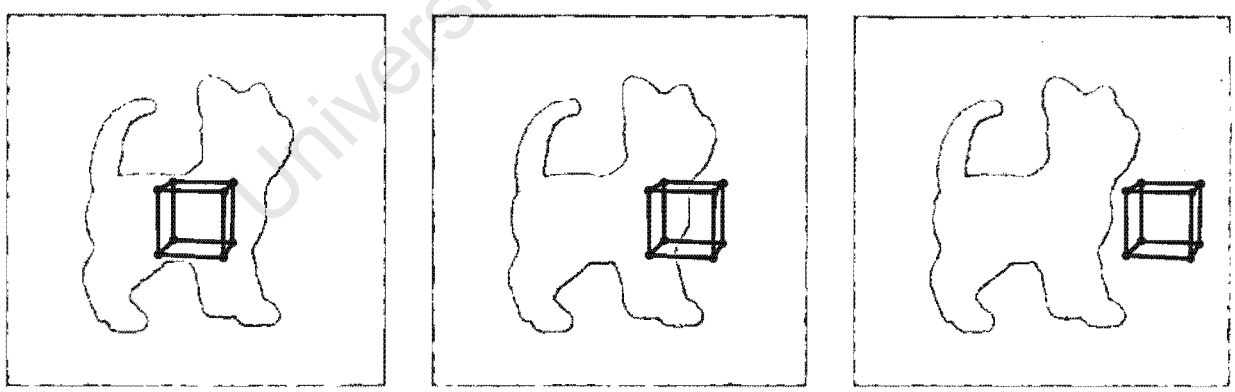

(a) Full Voxel (b) Partial Voxel (c) Empty Voxel

Figure 5.4: The three different voxel occupancy categories are shown. A white target is shown against a grey background with the perspective projection of a voxel shown in black. Image (a) shows a voxel fully enclosed by the target. Image (b) depicts a partially intersected voxel and image (c) shows an empty voxel that is completely outside the target.

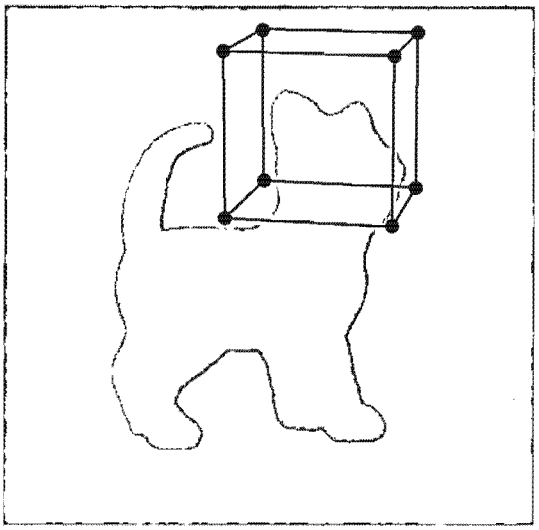

Figure 5.5: This figure illustrates how the following voxel is incorrectly categorised as being background due to none of the corners touching the target. A white target is shown against a grey background and the perspective projection of a voxel is shown in black. In the image, it is quite obvious that the voxel contains part of the object.

5.2 Octree Voxel Representation

The octree structure is ideal for representing the voxel-based visual hull model [1] and allows the storage of the 3D data to be compressed, making it possible to speed up the manipulation and display of the visual hull. An octree is a tree data structure in which each non-leaf node has at most eight child nodes. It is commonly used in computer graphics to provide a volumetric representation of an object. In this case, each node in the tree represents a voxel. The root node of the octree consists of a single large voxel that defines the bounding volume of the object. This voxel is known as the *universe cube*. Its centre must be as near as possible to the centre of the visual hull and must enclose the entire visual hull. Sections not part of the visual hull are iteratively "carved away" from the universe cube [18].

The octree structure stores a compressed version of the cuberille grid shown in Figure 5.2. If all eight of a voxel's child nodes are of the same occupancy category, the parent voxel adopts the category for itself. It is unnecessary to store these child nodes.

Initially the universe cube is subdivided in to eight smaller voxels (sub-octants). After this, only voxels with an occupancy of *partial* are subdivided until some predefined limit is reached. This limit is known as the *maximum subdivision level* and determines the resolution of the model. Generally, a larger maximum subdivision level results in a more refined and accurate model. The trade-off for a higher resolution model is the amount of processing time required to compute the model.

Voxels at the maximum subdivision level would normally be assigned an occupancy of *partial*. However, in this case they are uniformly assigned an occupancy of *full*, meaning that the surface of the actual object passes through all exterior surface voxels.

A simple volume is represented using the octree structure in Figure 5.6. The universe cube has been subdivided twice. Each node represents a voxel and the colour of the node indicates the occupancy of the voxel it contains:

- **Black** : The voxel is *full* and completely enclosed by the visual hull.
- **Grey** : The voxel is *partial* and lies on the surface of the visual hull.
- **White** : The voxel is *empty* and is completely outside the visual hull.

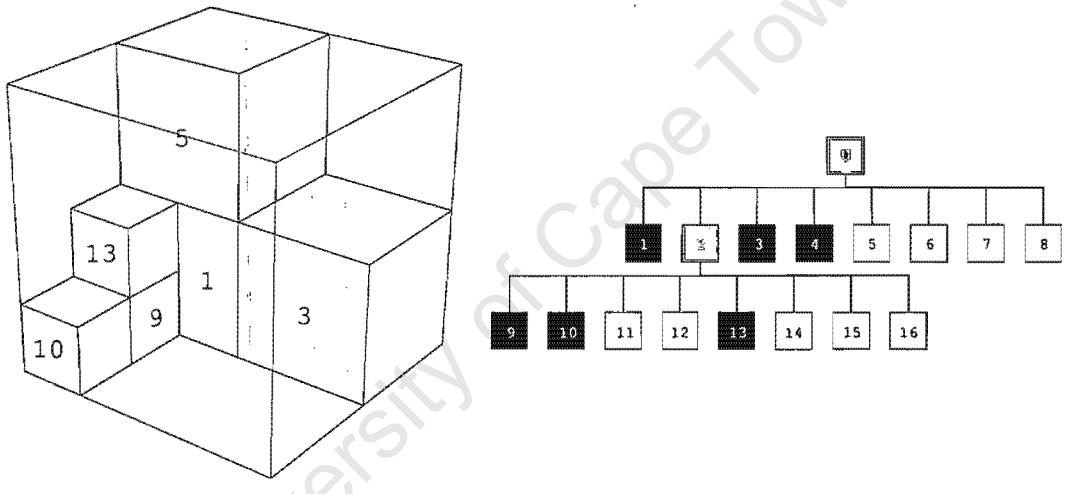

Figure 5.6: A simple volume represented by an octree and the corresponding tree structure with nodes. Each node in the tree is assigned one of the 3 colours (black, grey and white) according to its occupancy. A black node represents a voxel which is totally occupied, a grey node represents a voxel which is partially occupied, and a white node represents a voxel which is completely empty. Note that both black and white nodes do not have any child node, and hence they are leaf nodes in the tree. A grey node is an interior node in the tree, which has child nodes with different colours. It represents a voxel which lies on the boundary (surface) of the object [34].

Figure 5.7 illustrates how the accuracy of the visual hull can be improved by increasing the number of subdivisions. The first visual hull was computed with two subdivision levels, the second with three and the third with four. Upon inspection, it is obvious that as the number of subdivisions increase, so the visual hull becomes a better approximation of the object. The visual hull with four subdivision levels is the most accurate representation of the three. This model took the longest to compute.

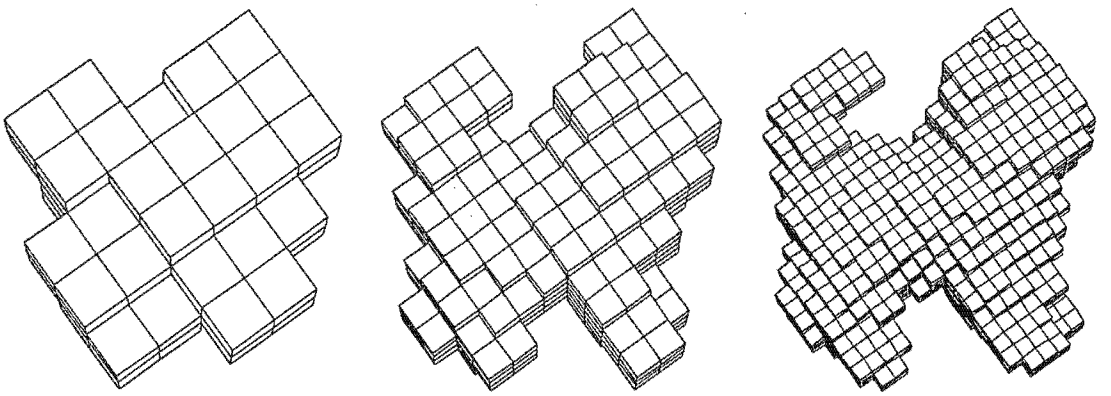

(a) Two Subdivision Levels (b) Three Subdivision Levels (c) Four Subdivision Levels

Figure 5.7: Three voxel-based visual hull models of the imaged cat from Figure 4.1 at three different subdivision levels. Model (a) is a very coarse model. An improvement in accuracy is clearly noticeable as the number of subdivision levels increase.

5.2.1 Data Compression

So far, voxels are subdivided until the maximum subdivision level is reached. Each leaf node in the octree structure represents a *full* voxel on the surface of the visual hull, which is at the maximum subdivision level. The octree structure allows for data compression in cases where all eight of a parent's child nodes have the same occupancy category. In such cases, the parent node assumes the occupancy of its children. The children are no longer required and can be deleted.

It is not efficient to generate the octree first and then check for nodes that have all 8 children with the same occupancy. Instead, a *minimum subdivision level* parameter is specified. Voxels positioned on levels between the root node and the minimum subdivision level are automatically assigned *partial* occupancy and subdivided further. Voxels occurring after the minimum level are only subdivided if their computed occupancy is *partial*.

Projecting all vertices belonging to the universe cube into the silhouette images, results in the cube being classified as *empty*. This is because the universe cube is chosen so that it completely encloses the object. The minimum subdivision level parameter accommodates for this and overrides the universe cube's occupancy with *partial*.

The use of a minimum subdivision level results in compressed data and reduces computational expenses. Setting the minimum level too high causes the speed of the system to increase.

Chapter 6

Surface Approximation using Marching Cubes

In a voxel-based visual hull model, the surface of the visual hull is coarsely represented by a number of small cubes. Using a polygon to represent a surface is smoother and more appropriate.

The marching cubes idea is more easily illustrated by its 2D equivalent, *marching squares*, in section 6.1. A more in-depth description of marching cubes follows in section 6.2. The standard MC15 algorithm[18] does not guarantee topological consistency and hence, improvements to the algorithm (MC33) are also discussed.

6.1 Marching Squares

The marching squares algorithm is based on the assumption that there are only a finite number of ways that a contour can pass through a square cell.

A simple contour can be approximated in a number of different ways. Standard sampling techniques store discrete measurements of a contour in a single dimension. Reproducing the contour is a matter of connecting the points measured with line segments. By sampling in multiple dimensions, the amount of information is increased and the accuracy improved. This is illustrated in Figure 6.1 (a) and (b) where the function $f(x) = \sin(x)$ has been sampled, first along a single axis and then along both axes.

The marching squares algorithm uses a similar concept to sampling along two axes. It divides the 2D plane into square cells in a grid-like structure. The four vertices of each square are

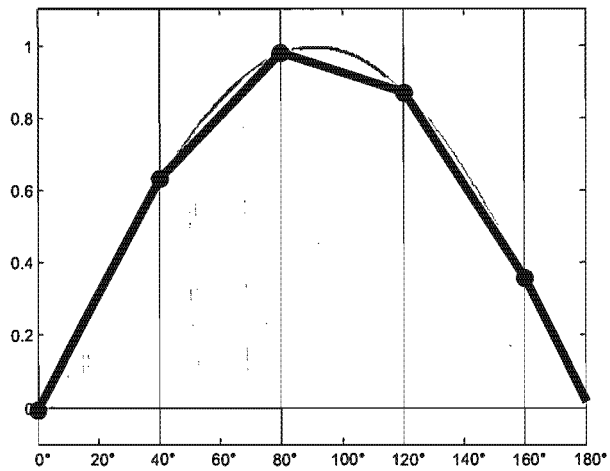

(a) Sampling in a Single Dimension

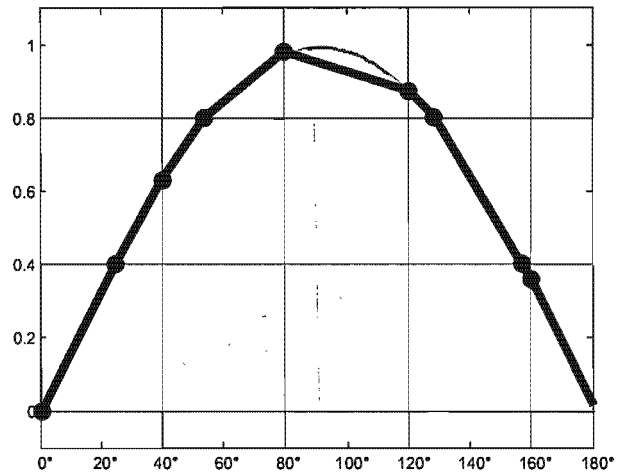

(b) Sampling in Two Dimensions

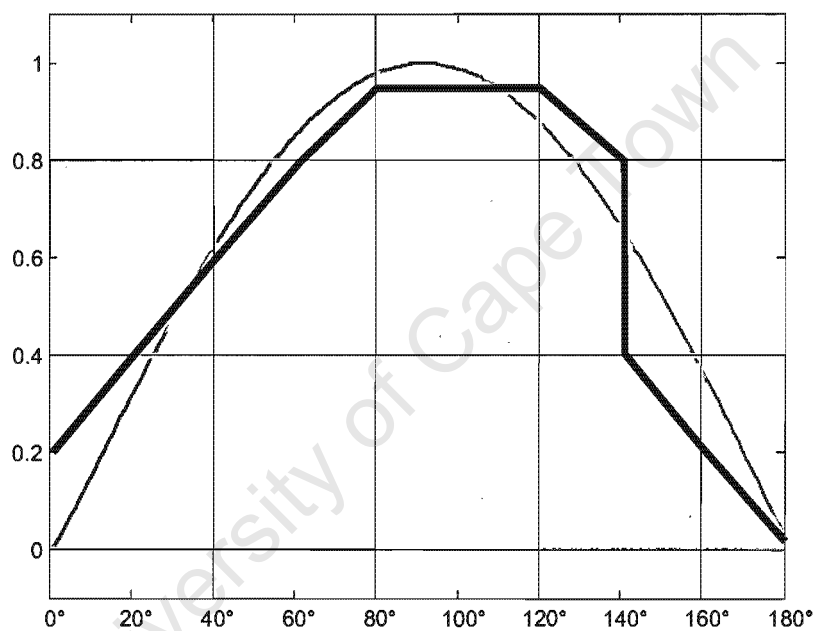

(c) Marching Squares Representation

Figure 6.1: The function $f(x) = sin(x)$ is sampled using three methods and shown by a grey area. In graph (a), the x dimension is sampled, while in plot (b), both x and y axes are sampled. Black dots indicate the samples and the curve that these samples represent is shown by a black line. Plot (c) shows how the marching squares would represent the curve.

assigned a binary value (either 0 or 1) by testing to see if they are outside or inside the shape being approximated. With the four vertices each having only two states, there are $2^4 = 16$ unique vertex configurations. The vertex values of a square form a binary pattern that is used as an index to look-up the line segment associate with that pattern. Figure 6.2 shows the 16 vertex patterns and their corresponding line intersections. The function $f(x) = \sin(x)$ is approximated using the marching squares algorithm in figure 6.1. Figure 6.3 shows how this concept is extended to

improve the 2D voxel-based visual hull.

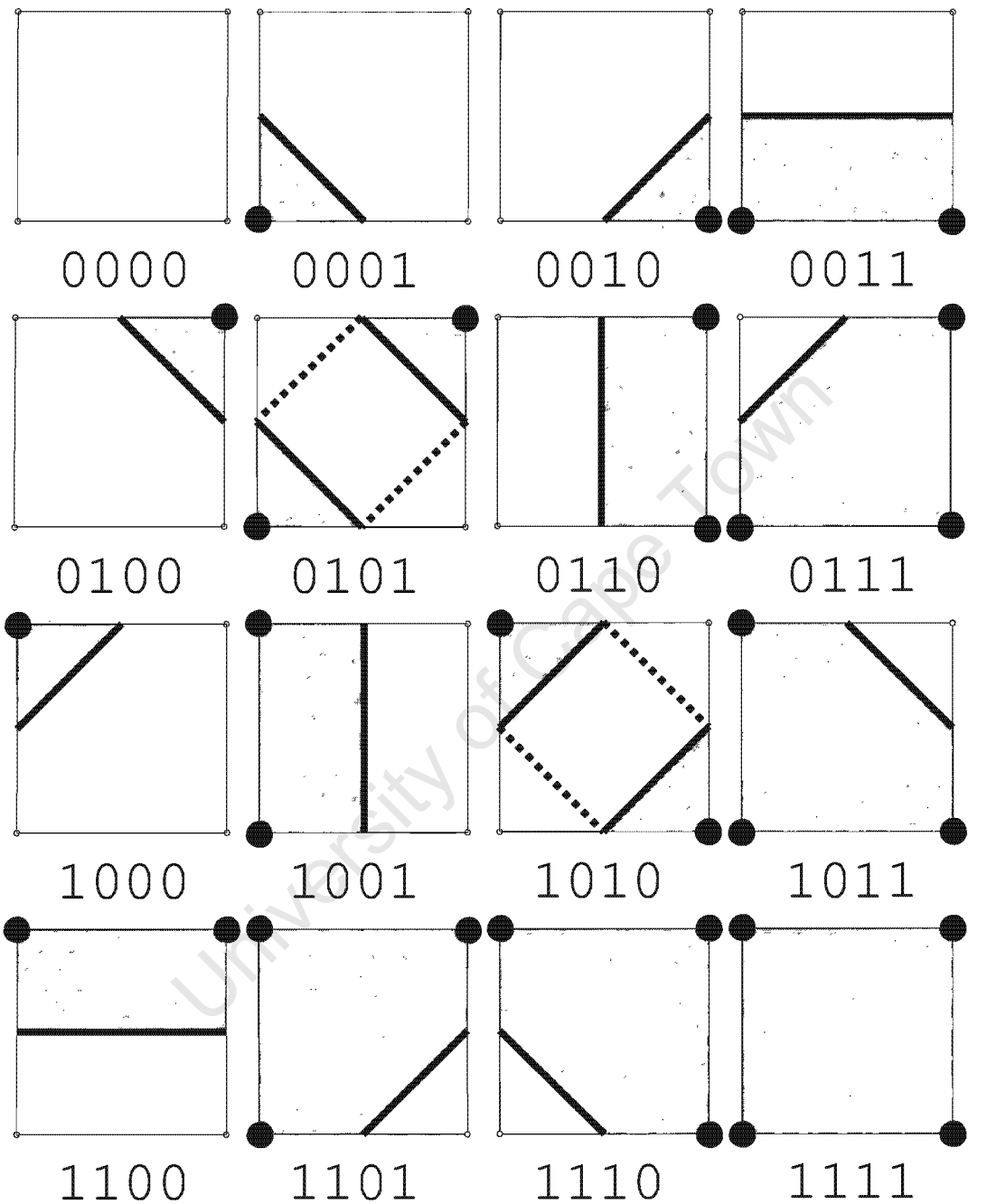

Figure 6.2: The marching squares look-up table. Solid black circles indicate that a vertex projects to inside the target, while the absence of a circle indicates that a vertex projects to background. Thick black line segments approximate the intersection with the target. The dotted lines shown for cases 0101 and 1010 indicate an ambiguous situation.

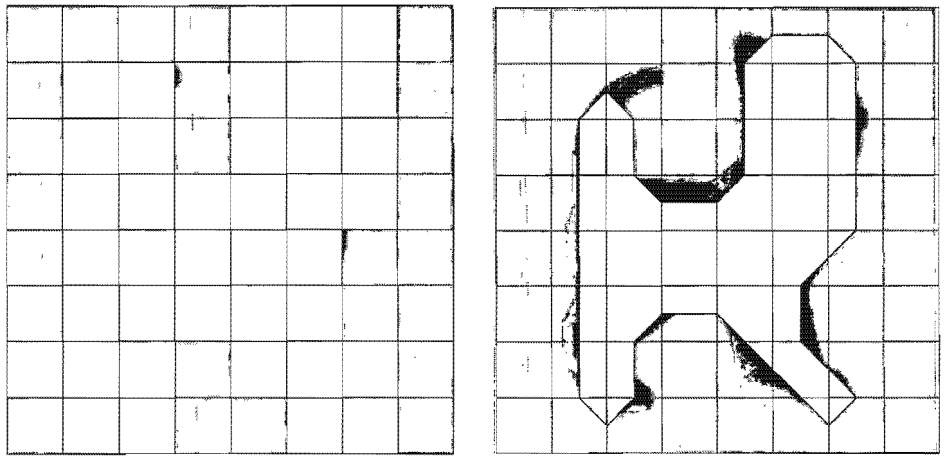

(a) (b)

Figure 6.3: In this illustration, squares in 2D correspond to voxels in 3D and the 2D target object is equivalent to the actual 3D visual hull. In each illustration, the universe square has been subdivided 3 times. A white fill indicates the computed 2D hull while.

6.1.1 2D Ambiguities

A closer examination of the table in Figure 6.2 shows that the two square with vertex configurations 0101 and 1010 cannot conclusively assign a specific arrangement of line segments and is ambiguous. This can result in holes in the 2D hull.

For this reason, the concepts of *separated* and *non-separated* points are introduced. Any two points with the same value that are connected through a path with the same value are non-separated. If such a path does not exist, the points are said to be separated. Figure 6.4 shows an example where two identical corner configurations are separated(a) and non-separated(b).

The separation information of points allows for the removal of ambiguous configurations. Ambiguous cases only arise when diagonally opposite corners have the same value and adjacent corners have opposite values. A test is used on squares falling into ambiguous categories, which checks the separation of corners. Ambiguities are also a problem in 3D and can be overcome using similar techniques.

6.2 Marching Cubes

The *marching cubes* algorithm is based on the assumption that there are only a finite number of ways that a surface can pass through a cubic cell.

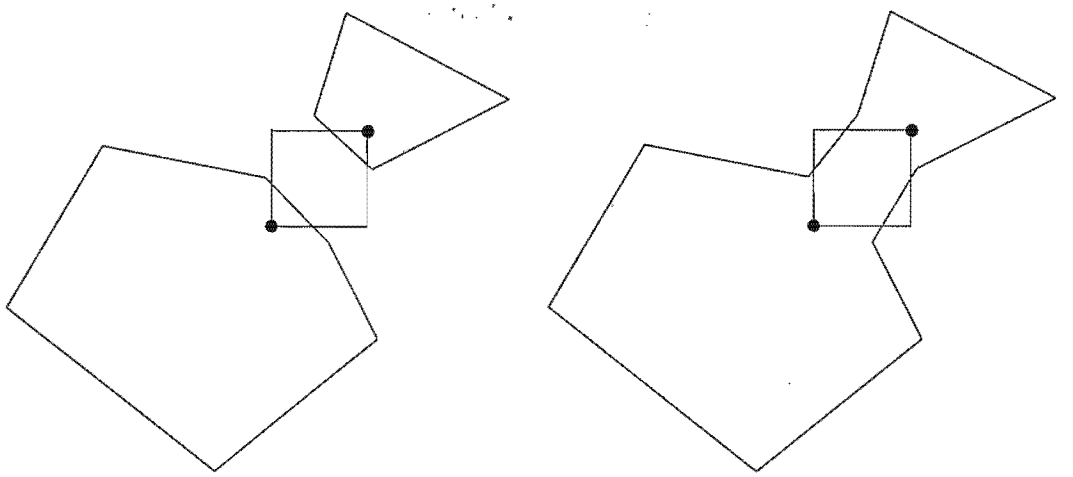

(a) Separated Corners (b) Non-Separate Corners

Figure 6.4: In both images, the target is represented in grey. The left hand target is made up of two parts, while the right hand target has only one. The squares in both images have the same corner configurations, but are obviously different. Testing the centre of the square would resolve the ambiguous situation.

Originally developed by Lorensen and Cline [18], MC15 provided visual access to experimental and theoretical data by producing a surface out of a sampled scalar field (cuberille grid). The method is adapted to represent the surface of a visual hull model. The surface of the object passes through all exterior voxels of the visual hull model. The surface passing through a single exterior voxel is approximated by tiling it with a set of triangular patches. The resultant visual hull is smoother than a voxel-based visual hull. High-frequency detail is also removed in marching cube visual hulls.

6.2.1 Approximating the Surface

The algorithm makes the assumption that all voxels in a cuberille grid are intersected by a surface of some sort. The type of surface is determined by considering a voxel's vertex values. The value of a vertex can be one of only two possibilities:

- *Full* : The vertex is part of the target.
- *Empty* : The vertex is part of the background.

With a voxel having eight vertices, and each vertex having only two states (*full* or *empty*), there are $2^8 = 256$ possible vertex configurations. The 256 cases are indexed using the numbering

system shown in Figure 5.3. The index is used to look-up a surface intersection given a certain voxel vertex configuration. Lorensen and Cline [18] made the assumption that each of the 256 cases implied a single unique surface intersection. Searching through a list of 256 possible states requires an unrealistic amount of processing time. It will be shown that by complementary and rotational symmetry, the 256 surface cases can be reduced to 15.

An inversion of all the vertex values of a voxel has no effect on the voxel's surface topology, other than an inversion of the surface normal (see Figure 6.5). Complementary symmetry makes it possible to reduce the number of surface cases to 128. With the addition of rotational symmetry, the cases are further reduced to 15.

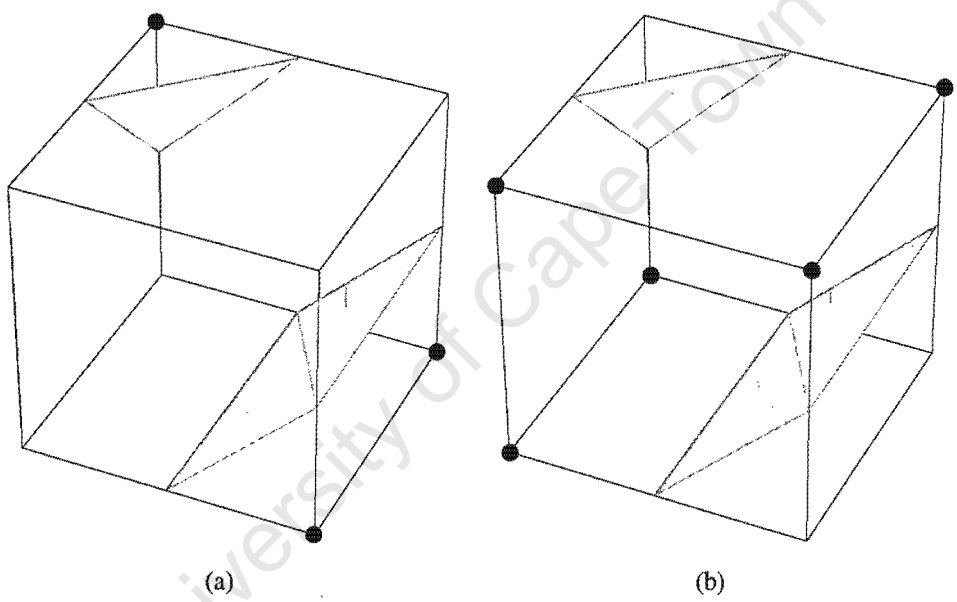

Figure 6.5: A voxel with a specific voxel corner configuration and its complement are shown. Solid black circles indicate *full* vertices. Both voxels approximate the surface intersection with the same triangle configuration.

Figure 6.7 shows a table, developed by Lorensen and Cline, of possible surface intersection that is used to map surfaces to each cube category. The surface cases are labelled 0 to 14. In the simplest case all vertices are *empty* (or inversely *full*), implying that it is not intersected by a surface. The 15 surface cases are incorporated into a surface look-up table that is indexed by the 256 voxel vertex configurations. To approximate the surface through a voxel with a random corner configuration, the corner index is computed and the appropriate surface is assigned.

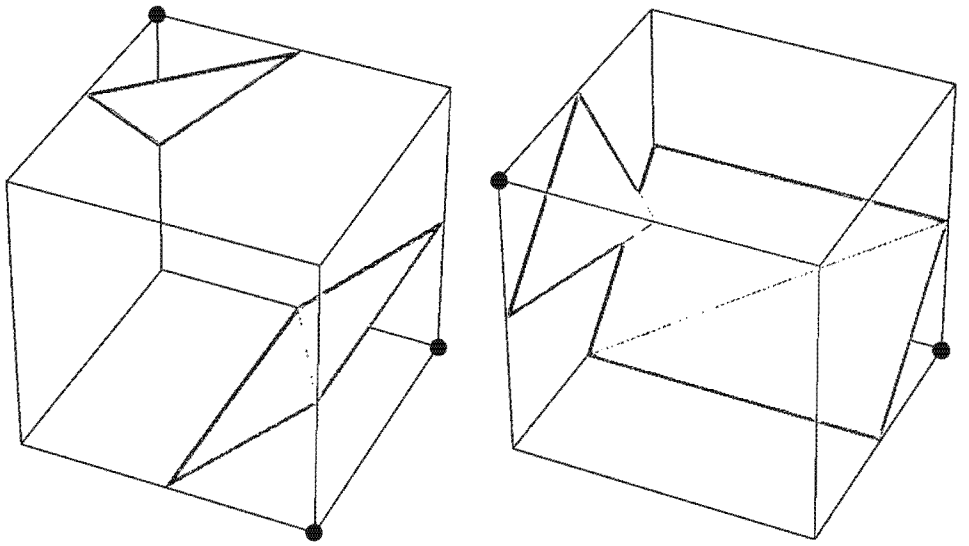

Figure 6.6: A voxel with a specific voxel corner configuration and a rotated version of the same voxel are shown. Solid black circles indicate *full* vertices. Both voxels are intersected by a rotated version of the same surface.

6.2.2 3D Ambiguities

It was found that Lorensen and Cline's surfaces do not guarantee topological consistency [24, 5, 23] and result in holes or cracks in the visual hull models, as seen in Figure 6.8(a).

Figure 6.9 illustrates three situations where two adjacent voxels have the same corner configurations. In cube configuration (a), the shared face has an obvious hole through it. The other two images suggest alternate configurations that would solve the error found in the first image.

It was discovered that, in seven of the 15 categories, a number of surface intersections possibilities had been overlooked. Using face tests initially introduced by Nielson *et al.* [24] and a new surface look-up table, Chernyaev [5] was able to solve these ambiguities with the MC33 algorithm. Chernyaev revised the surface look-up table of 15 to include 18 new surface cases resulting in 33 surface cases (see Figure A.1). In order to resolve surface ambiguities, the centre of shared faces or a voxel's centre is projected into all the silhouettes to test if they are part of the target or not. All the edges and faces of a voxel are numbered using the system shown in Figure 6.10. Table B.1 shows which points in the voxel need to be tested in order to decide the correct surface association. Using these tables, the ambiguous corner configurations are successfully resolved.

Figure 6.11 shows the effects of applying the MC33 algorithm to the voxel-based visual hull models in Figure 5.7. These models are smoother than the voxel-based versions from Figure

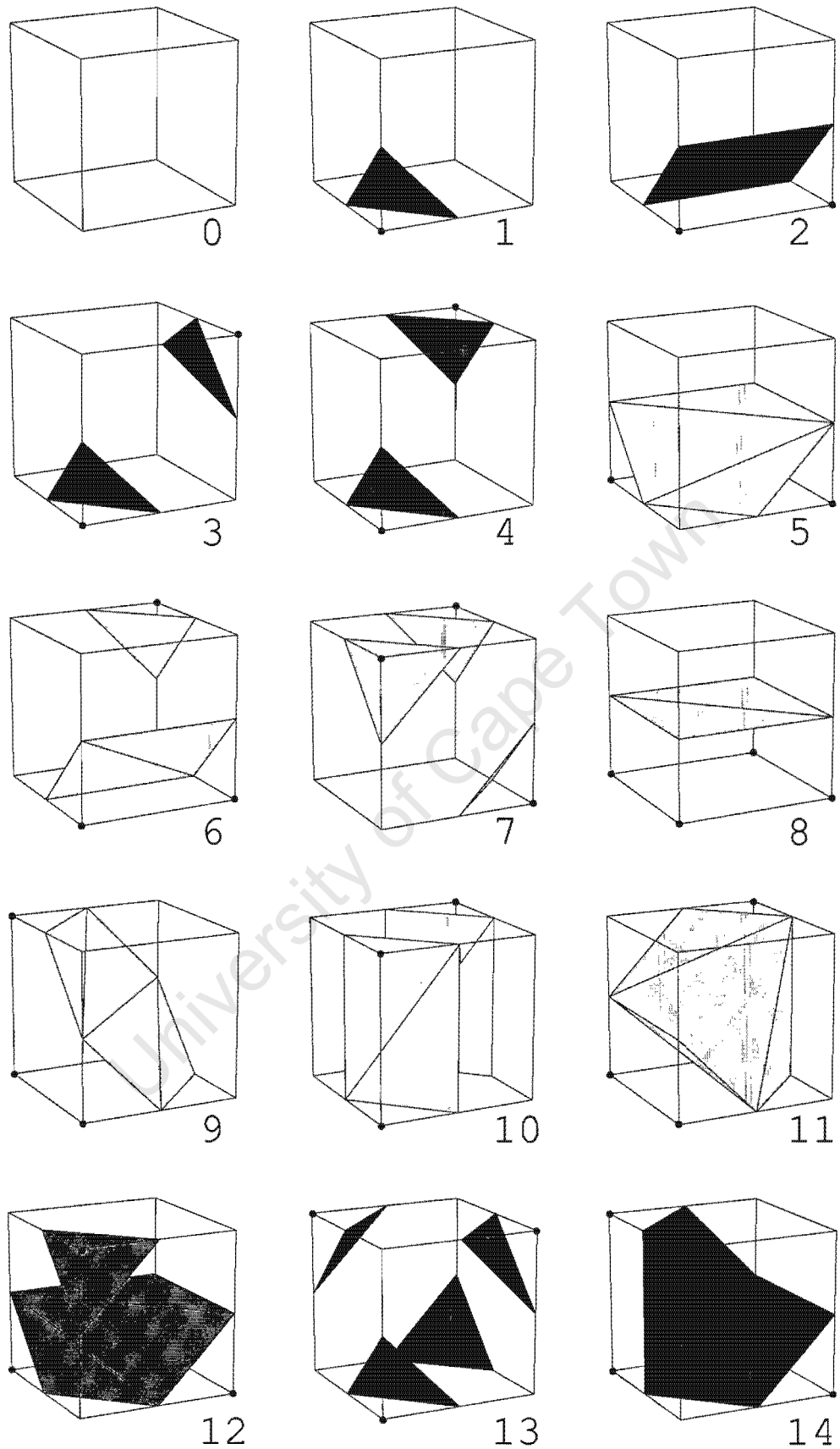

Figure 6.7: The MC15 surfaces first developed by Lorensen and Cline.

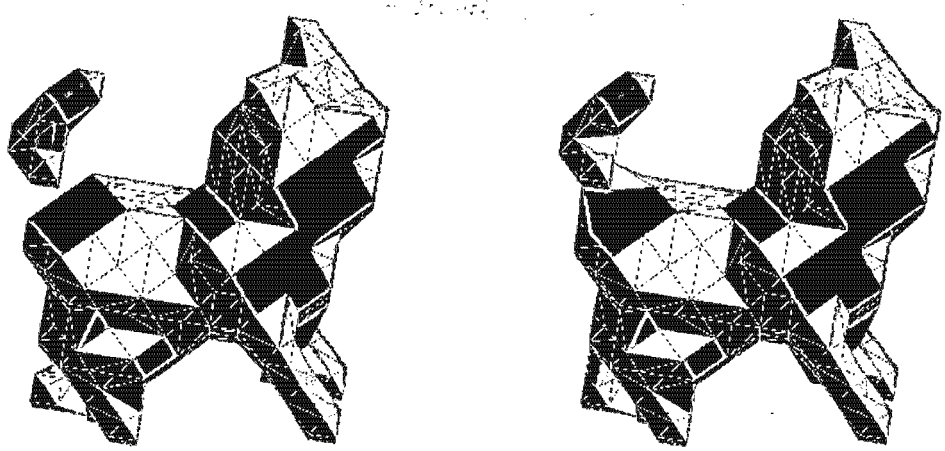

(a) MC15 (b) MC33

Figure 6.8: Cat (a) shows the effect of applying Lorensen's MC15 algorithm to the voxel-based visual hull model in Figure 5.7. Cat (b) shows the desired result without holes. The interior of the cat is red, making the holes more noticeable.

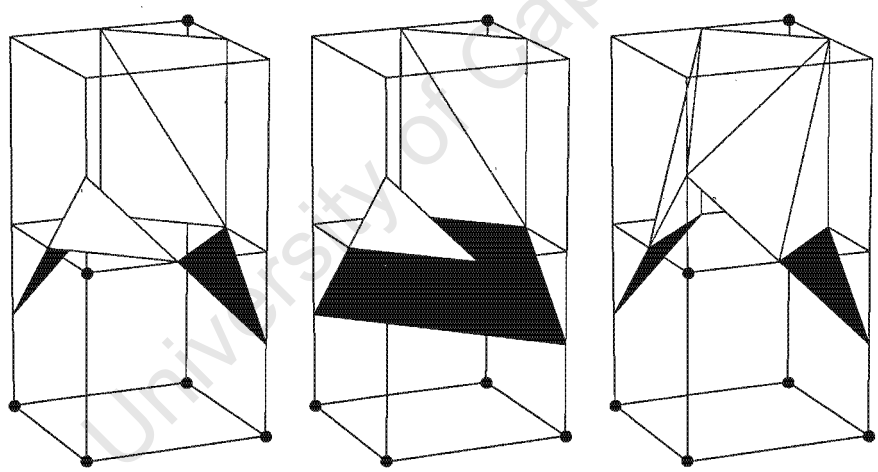

(a) (b) (c)

Figure 6.9: An example of an ambiguous marching cubes case. A cube from category 6 shares a face with the compliment of category 3. Cube (a) is assigned surfaces from the table of 15 in Figure 6.7, resulting in a hole through the shared face. This ambiguous situation is solved in the cube (b) and (c) topologies which use Chernyaev's 33 surfaces.

5.7. The patches are coloured according to their voxel vertex category. The improvement on the voxel model is quite evident in the middle marching cubes visual hull model.

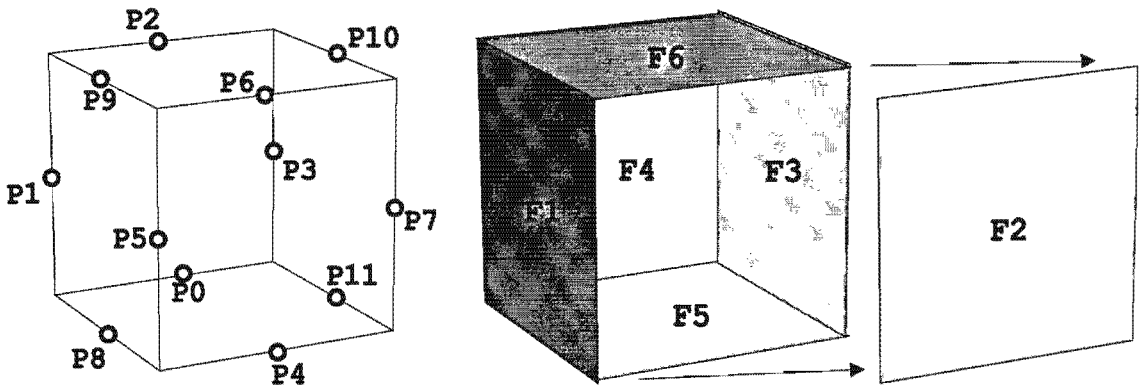

(a) Edge Labels (b) Face Labels

Figure 6.10: The labelling system used for the voxel's faces and its edges.

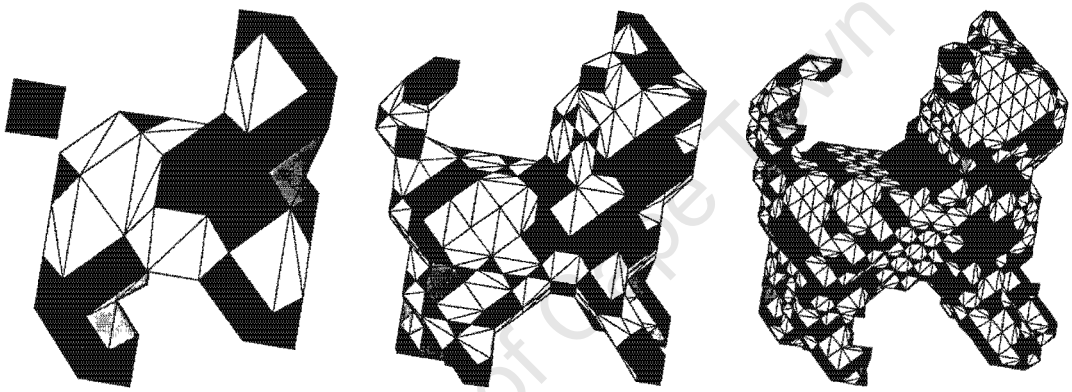

(a) Two Subdivision Levels (b) Three Subdivision Levels (c) Four Subdivision Levels

Figure 6.11: The 3D MC33 visual hull models of the imaged cat at increasing subdivision levels. Surface colours indicate from which category in Figure A.1 the surface is from.

6.2.3 Marching Cubes applied to an Octree Model

The surface passing through a voxel is approximated with the marching cubes algorithm. The surface of a voxel model appears coarse due to the sharp corners of each surface voxel. When the marching cubes algorithm is applied to an octree voxel model, the generated model's surface is closer approximation to that of the actual object. The marching cubes algorithm also reduces the size of the visual hull generated with the voxel model.

The marching cubes algorithm was developed for use with a standard cuberille grid. It individually scans each voxel, assuming that *all* voxels are the same size. In the octree voxel model, *full* voxels are not always the same size as they can be situated at different levels in the tree. Overlooking this flaw causes parts of the target's surface to be inconsistent, appearing as holes in the surface of a marching cubes visual hull. Setting the minimum subdivision level equal to the

maximum subdivision level solves the problem, resulting in higher computation times. This also means that the compression characteristics of the octree structure are not taken advantage of.

Chapter 7

Improving the Surface Estimate

The surface that passes through a voxel is approximated with the marching cubes algorithm. The accuracy, at which the marching cubes surface approximates the actual surface through a voxel, can be improved by applying single iterations of a binary search, along voxel edges, to the corners of each triangular patch. In this chapter, 2D analogies are made using the marching squares algorithm. The concept is then expanded to 3D.

7.1 A Binary Search in 2D

A binary search is an iterative process, based on "divide and conquer" principles, used to find a solution. The algorithm is used to search an ordered list by repeatedly dividing the search area in half. During an iteration the centre element is tested and the half of the list in which the desired element cannot lie is eliminated. Figure 7.1 illustrates the concept of a simple binary search. This algorithm normally runs until the desired value (or the closest value) is found.

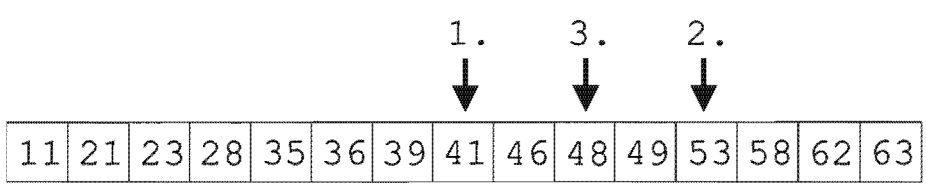

Figure 7.1: A random sequence of values is ordered from smallest to largest. A binary search tries to find the values closest to 47. The initial estimate is at the centre location, which corresponds to a value of 41. Arrows are used to indicate the iterations of the algorithm. After two iterations, the algorithm converges on a value close to 47.

The marching squares algorithm approximates the intersection of a 2D target with a cubic cell

by means of a line segment. Testing each end point of the line segment, to see if it lies inside or outside the target provides information that can be used in a binary search. Figure 7.2 shows the effects that a binary search has on a single square cell that is intersected by a target. Using the lookup table in figure 6.2, an initial line is used as a first approximation to the intersecting target. In each iteration the end points of the line segment are adjusted. The result is that the line ends are moved independently along the square's edge towards the corner with the opposite value to the line end, causing the line segment to be shifted closer to the actual target edge.

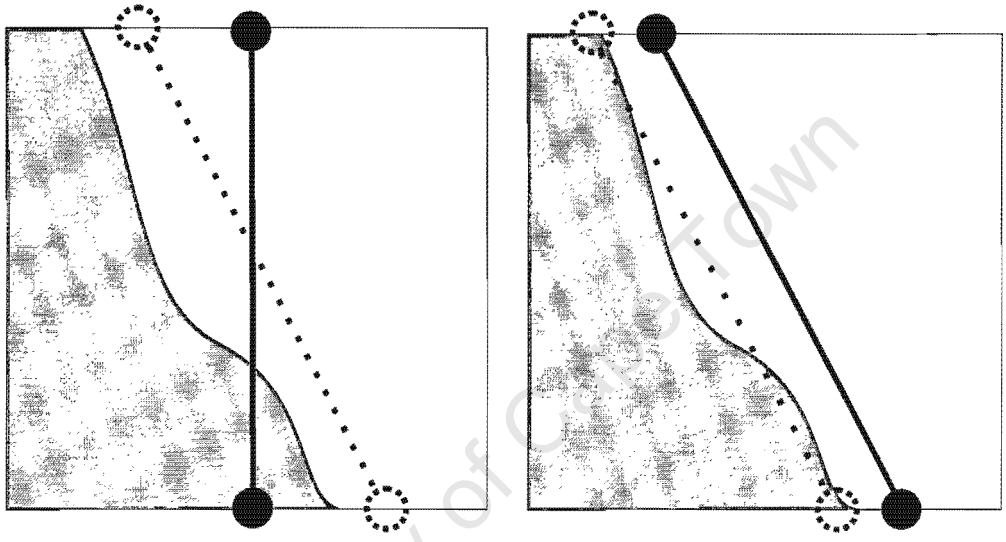

Figure 7.2: A square cell is intersected by a grey 2D target. Illustration (a) uses the marching squares table in figure 6.2 to obtain an initial estimate. The marching squares line segment is indicated by a solid line. The dotted line shows the position of the line segment after one iteration of a binary search. In illustration (b), the binary search uses the binary search estimate from (a) as its initial intersection. The dotted line is the result of a second binary search iteration.

Figure 7.3 illustrates the effects that each iteration of a binary search has on an initial estimate and shows how binary search iterations can improve the accuracy of the marching squares algorithm. In the figure, one of the front paws of the cat is not properly included in the 2D hull before or after the binary search has been applied. Here, the cell is intersected by a part of the target that is too curved in shape to be properly approximated by a straight line. A single iteration of the binary search results in better approximations of the intersecting target. The computational expenses increase with the number of binary search iterations.

(a) (b)

Figure 7.3: 2D Binary search sample. The squares in 2D correspond to voxels in 3D and the 2D target object is equivalent to the actual 3D visual hull. In each illustration, the universe square has been subdivided 3 times. A white fill indicates the computed 2D hull.

7.2 Searching along the Voxel Edge

The binary search algorithm described here is applied to each voxel individually and there is no concept of voxel connectivity. Many shared points are unnecessarily retested.

Each corner of every triangular patch associated with a voxel lies on an edge of the voxel. The voxel vertices that are connected by this edge will *always* be classified into opposite occupancy categories. The point at which the surface intersects the voxel lies along the voxel edge, between the two voxel vertices. The marching cubes algorithm approximates this point of intersection with a corner of each triangular patch.

The triangle's corners are projected into all the images and their occupancy is computed. The corners are then independently moved along the edges towards a vertex with the opposite occupancy value. This means that *full* corners are moved away from *full* voxel vertices and *empty* corners are moved away from *empty* voxel vertices. The distance that the triangle corner is moved is computed by halving the distance between corner and the nearest of the two voxel vertices.

The result of applying this binary search to the marching cubes visual hull from Figure 6.11 can be seen in the hull models illustrated in Figure 7.4. The effects are more noticeable in the first visual hull model, which has a lower number of voxel subdivisions. The higher the number of voxel subdivisions, the less noticeable the effects of the binary search become.

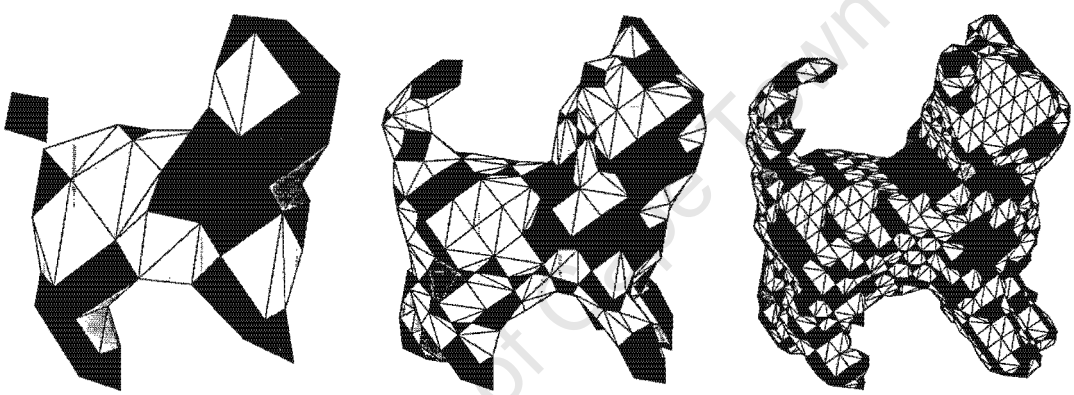

(a) Two Subdivision Levels (b) Three Subdivision Levels (c) Four Subdivision Levels

Figure 7.4: The 3D marching cubes visual hull models of the imaged cat at increasing subdivision levels. Two iterations of a binary search have been applied. Surface colours indicate from which category in Figure A.1 the surface is from.

Chapter 8

System Overview

This chapter describes the hardware used to capture the images and discusses the actual implementation of the algorithm. All software was initially coded in MATLAB, and then recoded in the C++ programming language. The optimised code was placed inside a MATLAB executable (mex) wrapper so that it could be called from MATLAB's command line.

8.1 Image Acquisition

The multi-camera system was implemented due to its availability. Six standard fire-wire cameras were used to obtain test data, while a five camera system was used to capture images of the plastic cat used in the illustrations. The cameras were remotely triggered and synchronously captured grey-scale images at a resolution of 640×480 that were stored using in PNG (*Portable Network Graphics*) format. The images were not processed in real-time.

The five camera system is shown in Figure 8.1. This system was used to capture images of the small plastic cat used in most of the illustrations. Figure 8.2 shows the grey scale images this system generated.

8.1.1 System Calibration

The system was calibrated using an external program. The calibration procedure used a calibration object, machined out of metal, which was a scaled version of the calibration object shown in figure 3.1. Binary patterns were burnt on with a laser. A program developed by Keith Forbes [8] was then used to calibrate the system. Using multiple images of the calibration object, intrinsic

and extrinsic camera parameters for the system were calculated.

8.1.2 Image Segmentation

Sample grey-scale and silhouette images can be seen in Figure 8.2. The silhouettes were obtained by placing a threshold on the grey scale intensity values contained in the images. The different regions that resulted were labelled. The largest region was assumed to be the background, and marked as such. All other regions were marked as being part of the target. Binary morphological operators were applied to the silhouettes in order to smooth the edges.

8.1.3 Estimation of the Universe Cube

The universe cube is defined by two characteristics, the 3D coordinates of its centre and the length of one of its sides. The universe cube is required to be chosen so that it completely encloses the target.

In most of the images used, the target occupies less than 30% of the area of each image. It would have been better if the target was better matched to the camera's field of view and consumed around 50% of the image. Eighty percent of the larger image dimension (in this case the width) was used as the length of the sides of the universe cube.

The universe cube's centre is set so that it is near the centroid of the object. This is done to improve the chances that the object is completely enclosed by the universe cube. The position of the object's centroid is unknown, which requires an estimate of the visual hull's centroid to be made. It is assumed that the projections of 2D centroids in each silhouette intersect (or nearly touch) near the visual hull's centroid. This point is assumed to be close enough to the visual hull centroid, and therefore used as the centre of the universe cube.

8.2 The Final Algorithm

The following sections contain a description of the Voxel Generation, marching cubes and binary search algorithms that were implemented in this process. Each system builds on the previous one. All of them created an octree of voxels. The marching cubes algorithm then used the voxels to create the marching cubes surfaces, and the binary search was subsequently applied to the marching cubes surfaces.

8.2.1 Voxel Generation Algorithm

A flow chart of the entire voxel algorithm is shown by the diagram in Figure 8.3. The inputs to the system are the silhouette images and the calibration data.

The 3D coordinates and dimensions of the universe cube are first calculated. The level of the universe cube is set to 1. Each child node has a level that is one more than its parent node's level. If a voxel's level is greater than the maximum level (or resolution), no more computations on the voxel are required.

The minimum level is checked against the voxel's current level. This level decides the point until which voxels are automatically assigned an occupancy of *partial*.

The vertices of the voxel are projected onto each silhouette image and tested using the previously described criteria. Each voxel vertex value is stored for later use in the marching cubes algorithm. If a voxel is marked as *full* or *empty*, no more computations on the voxel are required. Any voxel that does not fall into one of these first two categories is *partial* and is subdivided into eight child node voxels. The process then loops until one of the *exit* states. The voxels in this implementation used linked lists to accommodate pointers to their eight child voxels. These eight pointers are required in order to implement the octree data structure described in a previous section.

The output from this algorithm is a list of voxels described by a four column matrix. The first three columns contain the 3D coordinates of the centre of the voxel, and the last column contains the length of one edge of the voxel. A rendered sample output can be seen in Figure 8.4.

8.2.2 Marching Cubes Algorithm

For each voxel in the voxel-based model, the marching cubes algorithm goes through the following four steps[16]:

1. Determine the case number and configuration of the voxel;
2. Look up which faces are to be tested for this configuration;
3. Determine the subcase based on the result of the face tests;
4. Look up the tiling of the cube for this subcase.

The algorithm relies on three lookup tables:

- The case table maps each of the 256 possible configurations of a cube to one of the 15 cases of figure 2, and to a specific index number designating this configuration.
- The test table stores the tests to be performed to resolve topological ambiguity for each configuration.
- The tiling table stores the tiling for each configuration and subcase. It normally consists of a list of triangular patches.

The marching cubes algorithm relies on an accurate voxel model as an input. Other input data is obtained from the three tables mentioned above. A description of the flow chart, shown in Figure 8.5, follows. The root voxel node is initially selected. The algorithm checks if the voxel has children. Voxels are then iterated through until a leaf voxel node is found. This process has been drastically simplified, as it does not add much value to the internals of the algorithm. The reason for this is that all leaf voxels are found on the surface of the visual hull. The voxels index is computed. The index code is then searched for in the case table. If the index code is not found, the voxel is iteratively rotated about the x, y and z axis until a matching index entry is found in the case table. The number of rotations about each axis is stored for later use. Voxels with topological ambiguities are further tested until the ambiguity is resolved. Table B.1, in the appendices, lists the face or interior tests that are required to resolve any ambiguous cases and maps each case to it's appropriate surface configuration in figure A.1 (Figure A.1 can also be found in the appendices). The table refers to faces that have been labelled according to figure 6.10. The tiling table is then used to assign the appropriate surface to the voxel. Using the stored rotation values, the orientation of the surface is then aligned with that of the voxel. It is at this point that the binary search is applied to the vertices of each triangular patch that makes up the voxel's assigned surface. The section that follows describes this process in more detail.

The output of this algorithm is a list of triangles in a $9 \times n$ matrix, where n is the number of triangular patches. Each row contains the (x, y, z) coordinates for a patch's three vertices. Vertices are ordered anti-clockwise about the surface normal (using the *right hand rule*). Rotating views of a sample marching cubes output can be seen in Figure 8.6.

8.2.3 Vertex Binary Search Algorithm

This section of the algorithm applies a binary search to the vertices of each of the triangular patches making up the surface assigned to a voxel. It takes, as input, a list of between 0 and 9 triangles, depending on the surface associated with that particular voxel. A flow chart of this algorithm is shown in Figure 8.7. The images and calibration data is also made available to the algorithm.

The user defines a number of times that the binary search will be executed. All triangular patch vertices lie on a voxel edge. Each vertex is evaluated individually. End points of the voxel edge, on which a vertex lies, are projected into the silhouette images so that their occupancy can be computed. In *all* cases, one of the ends will have an occupancy of *full* and the other, *empty*. The occupancy of the current vertex being evaluated is also computed. The concept uses the rule that the opposite occupancy value of an end point attracts the vertex towards it. This means that *full* vertices are moved away from *full* end points and *empty* vertices are moved away from *empty* end points. The distance that the vertex is moved is computed by halving the distance between vertex and the nearest end point.

Figure 8.8 shows the visual hull of the small plastic cat that was computed from the five images in Figure 4.1 with the subdivision level set to 3 and the binary search set to 3.

8.3 Computing Visual Hull Volumes

Visual hull volumes were computed so that a comparison of efficiencies between the various methods could be made. These volume values are compared against ground truth measurements and provide a means to test the accuracy of the different systems.

8.3.1 Voxel Model Volume Computation

A voxel is a cubic volume of space and its volume is calculated by cubing the length of a side. Thus in a voxel-based visual hull model comprised of n voxels, where each voxel has a volume $V_n = s_n^3$ with s_n the length of the voxel's edges, the volume V_{vh} of the voxel-based visual hull model is the sum of volumes of the voxels that it comprises:

$$V_{vh} = \sum_{i=1}^{n} s_i^3. \tag{8.1}$$

8.3.2 Marching Cube Model Volume Computation

The method implemented to compute the visual hull volumes from a list of triangular surfaces was developed by Lien and Kajiya [17].

The determinant, T, is computed for each triangle using the following equation:

$$T = x_1(z_3y_2 - y_3z_2) + y_1(x_3z_2 - z_3x_2) + z_1(y_3x_2 - x_3y_2). \tag{8.2}$$

The three vertices that form the triangle always have the first triangle vertex (x_1, y_1, z_1) as their first vertex, followed by the ordered vertices (x_2, y_2, z_2) and (x_3, y_3, z_3). The volume V_{vh} of a polyhedron is given by equation 8.3.

$$V_{vh} = \frac{1}{6}\sum_{F_i} T \tag{8.3}$$

Face F_i consists of 3 edges and vertices are numbered from 1 to 3. The method can be extended to compute the centroid of the visual hull, situated at (x_0, y_0, z_0). The centroid is the centre of mass for a polyhedron of constant density and can be calculated using equation 8.4.

$$x_0 = \frac{1}{24V}\sum_{F_i} T(x_1 + x_2 + x_3) \tag{8.4a}$$

$$y_0 = \frac{1}{24V}\sum_{F_i} T(y_1 + y_2 + y_3) \tag{8.4b}$$

$$z_0 = \frac{1}{24V}\sum_{F_i} T(z_1 + z_2 + z_3) \tag{8.4c}$$

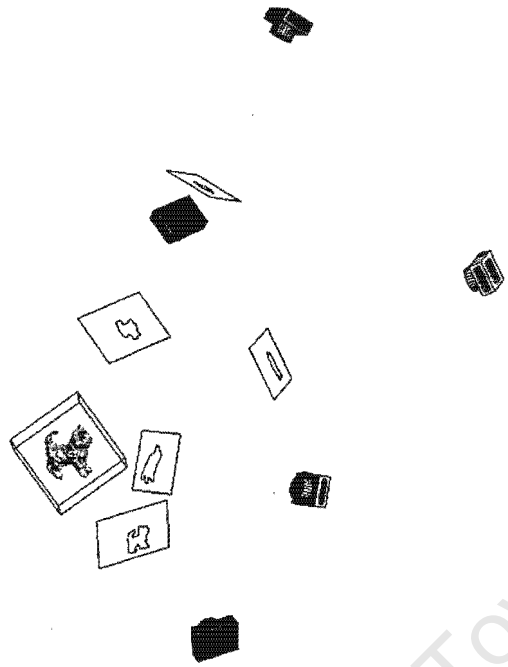

(a) The camera arrangement with respect to the cat. The universe cube completely encloses the cat.

(b) The visual cones are back-projected from each camera and the visual hull lies at the intersection of the cones.

Figure 8.1: Five cameras were used to capture the silhouette images of the small plastic Cat.

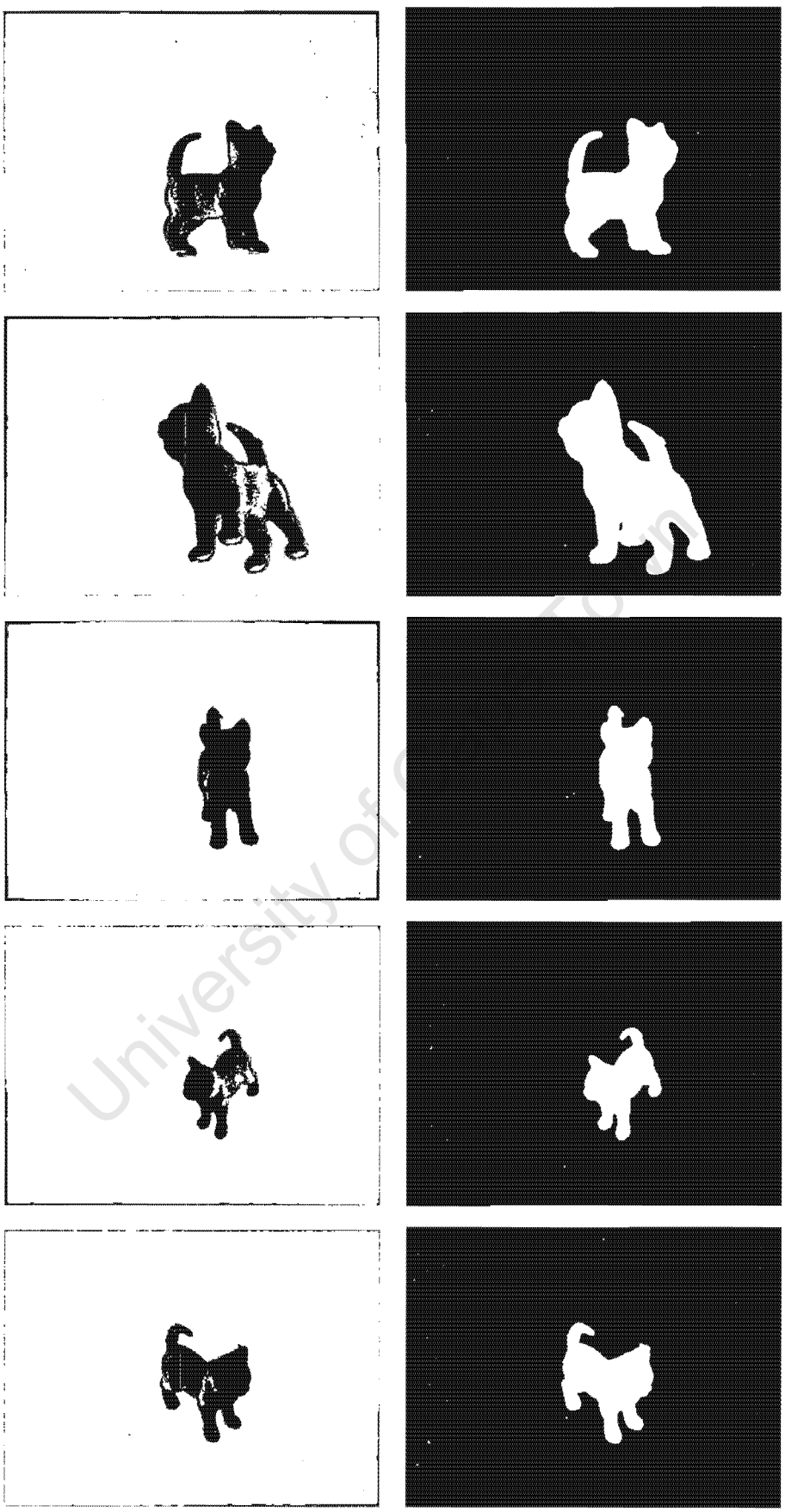

Figure 8.2: Five grey-scale and silhouette images of the small plastic cat generated using the camera system illustrated in 8.1.

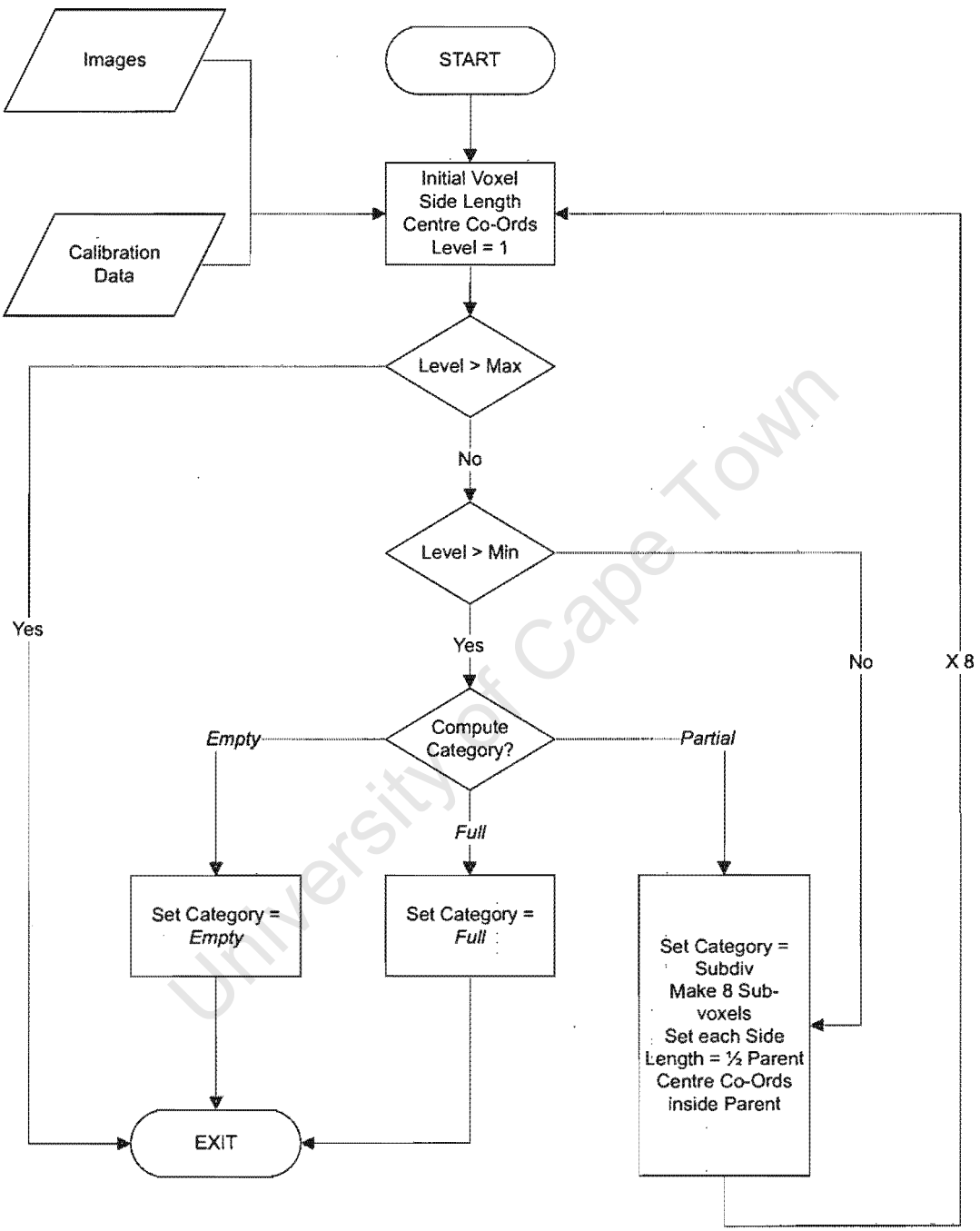

Figure 8.3: The voxel reconstruction algorithm flow chart.

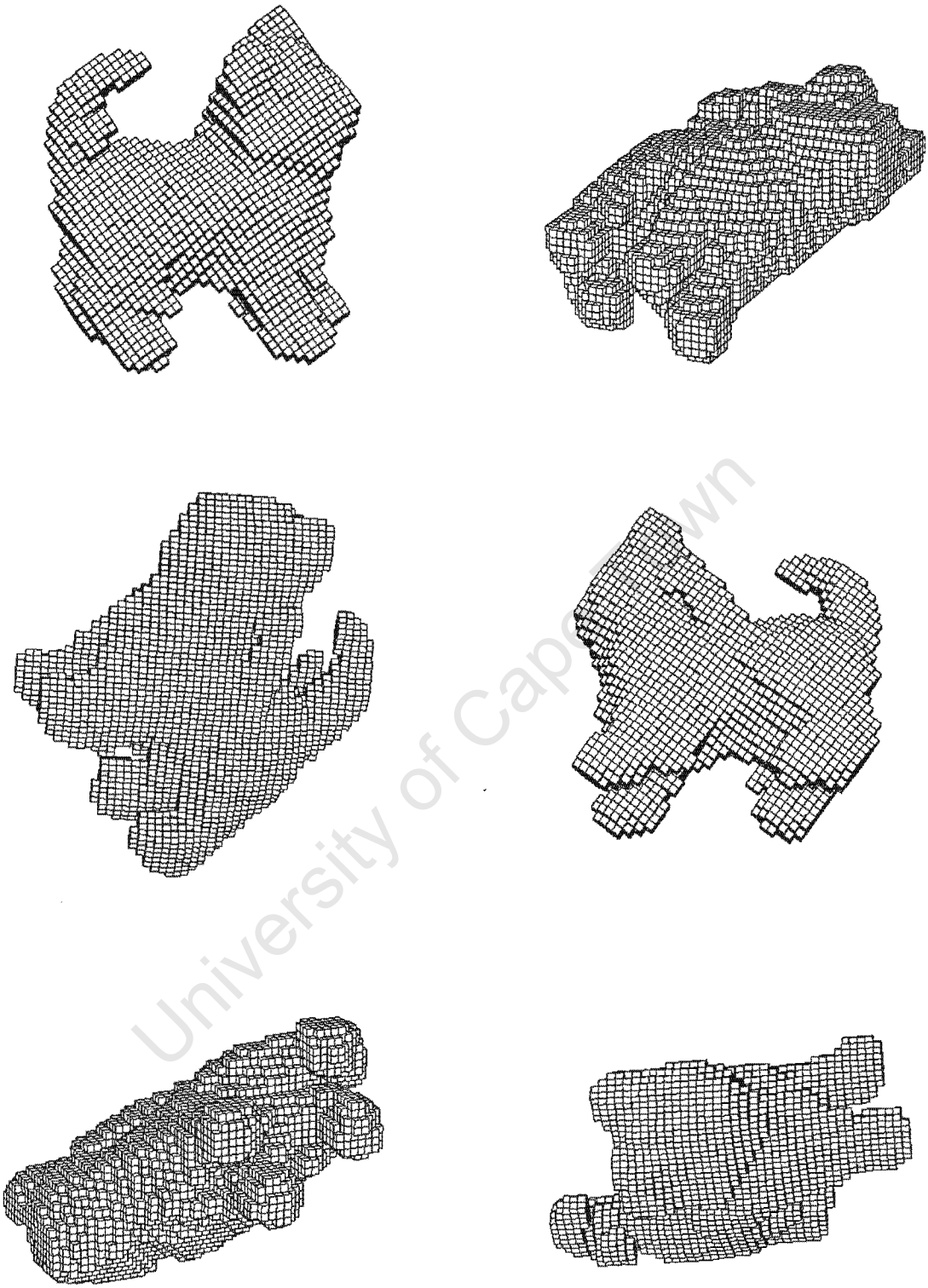

Figure 8.4: Six rotated views of a voxel-based visual hull reconstruction of the small plastic cat. The maximum subdivision level is set to five.

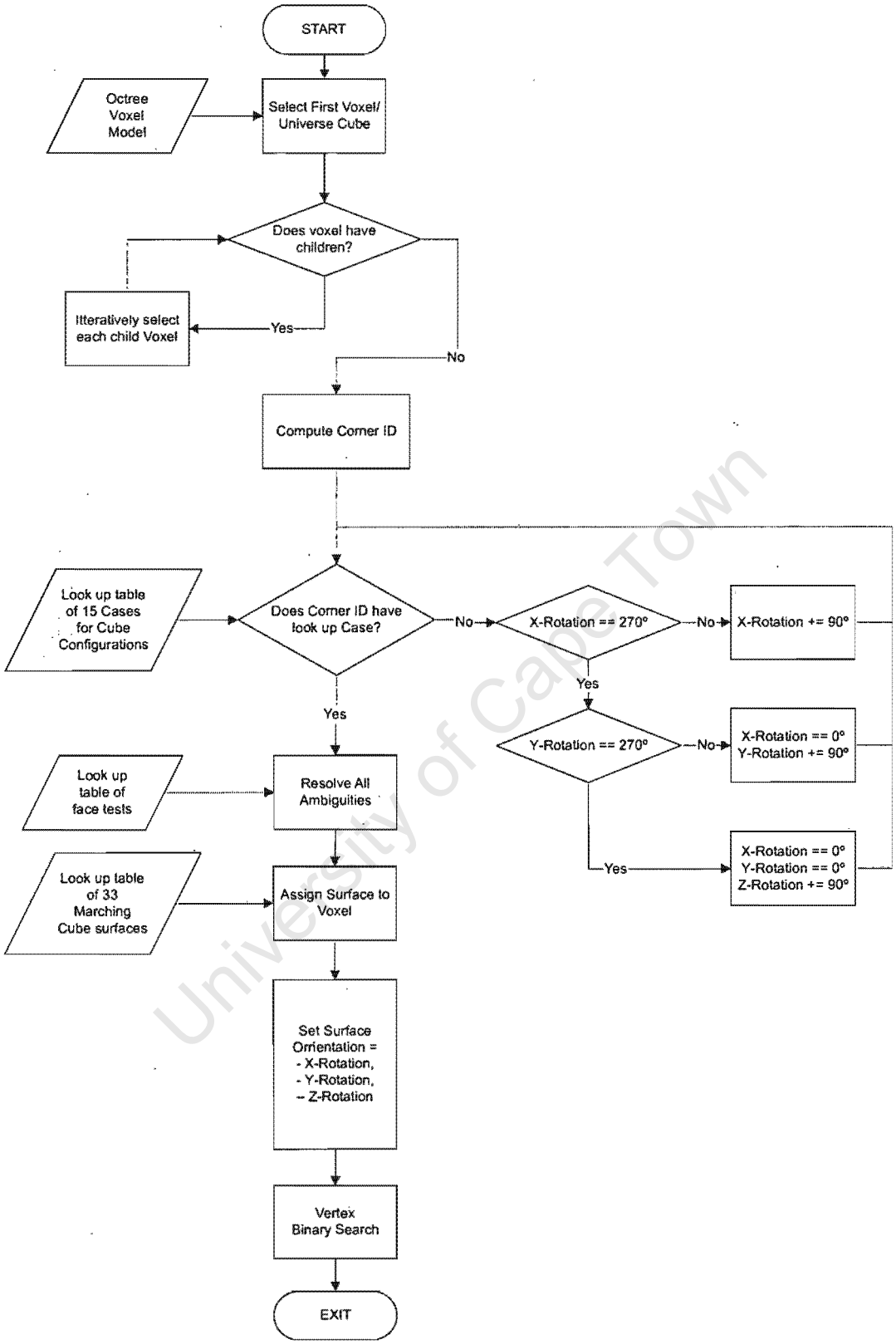

Figure 8.5: The marching cubes visual hull reconstruction algorithm flow chart.

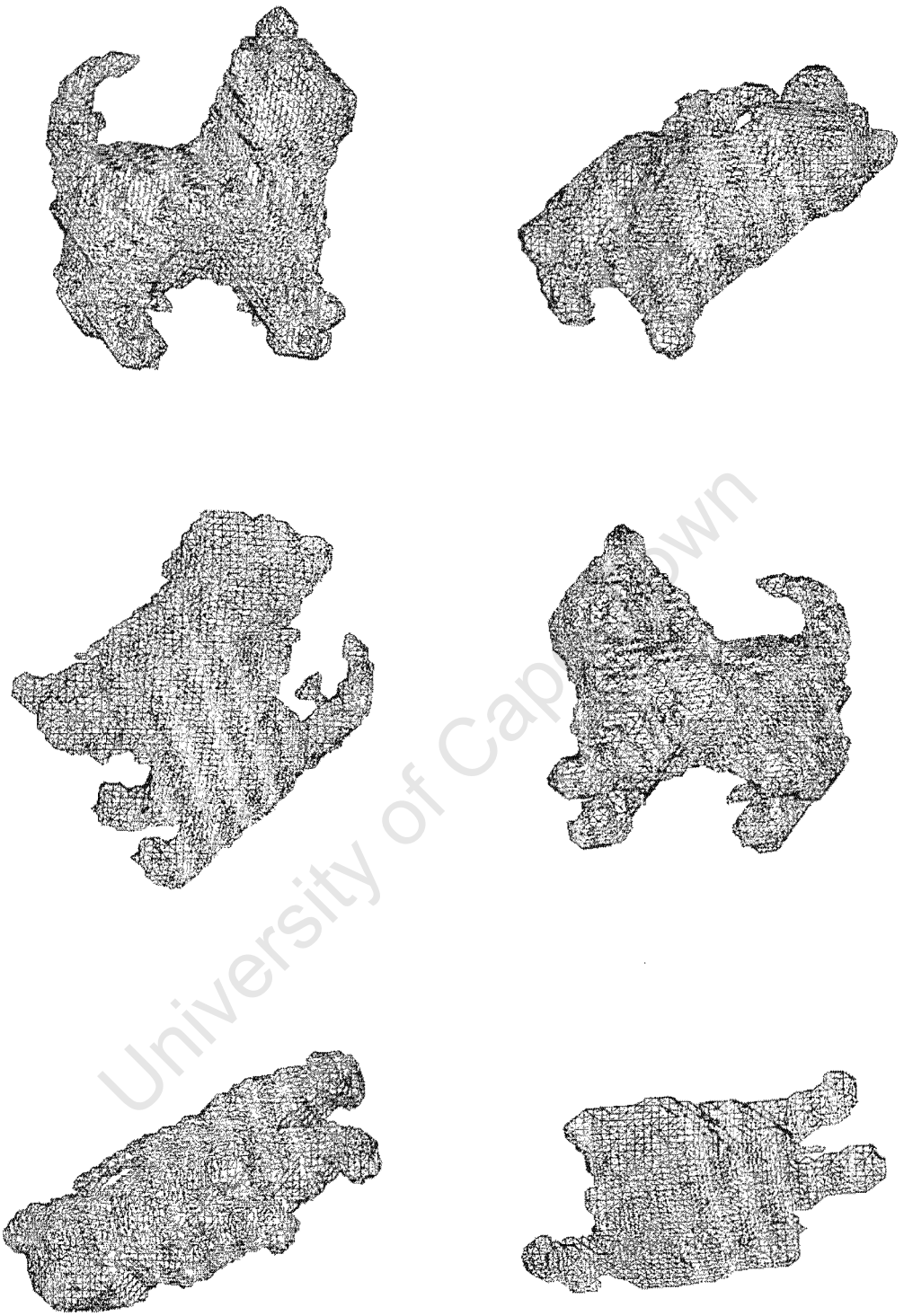

Figure 8.6: Six rotated views of a visual hull reconstruction of the small plastic cat. The model is made up of marching cubes surfaces. The maximum subdivision level is set to five.

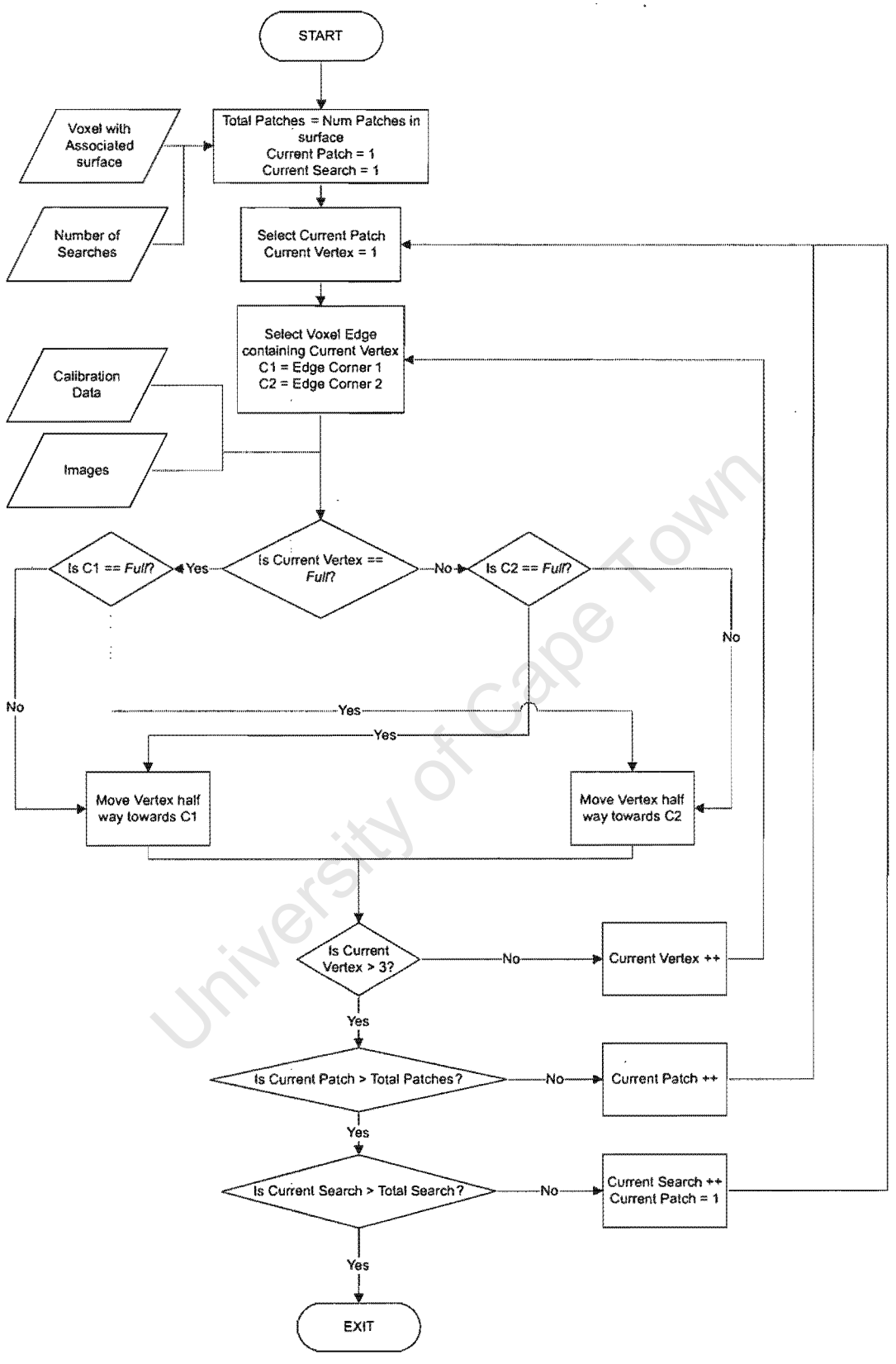

Figure 8.7: The vertex binary search algorithm flow chart.

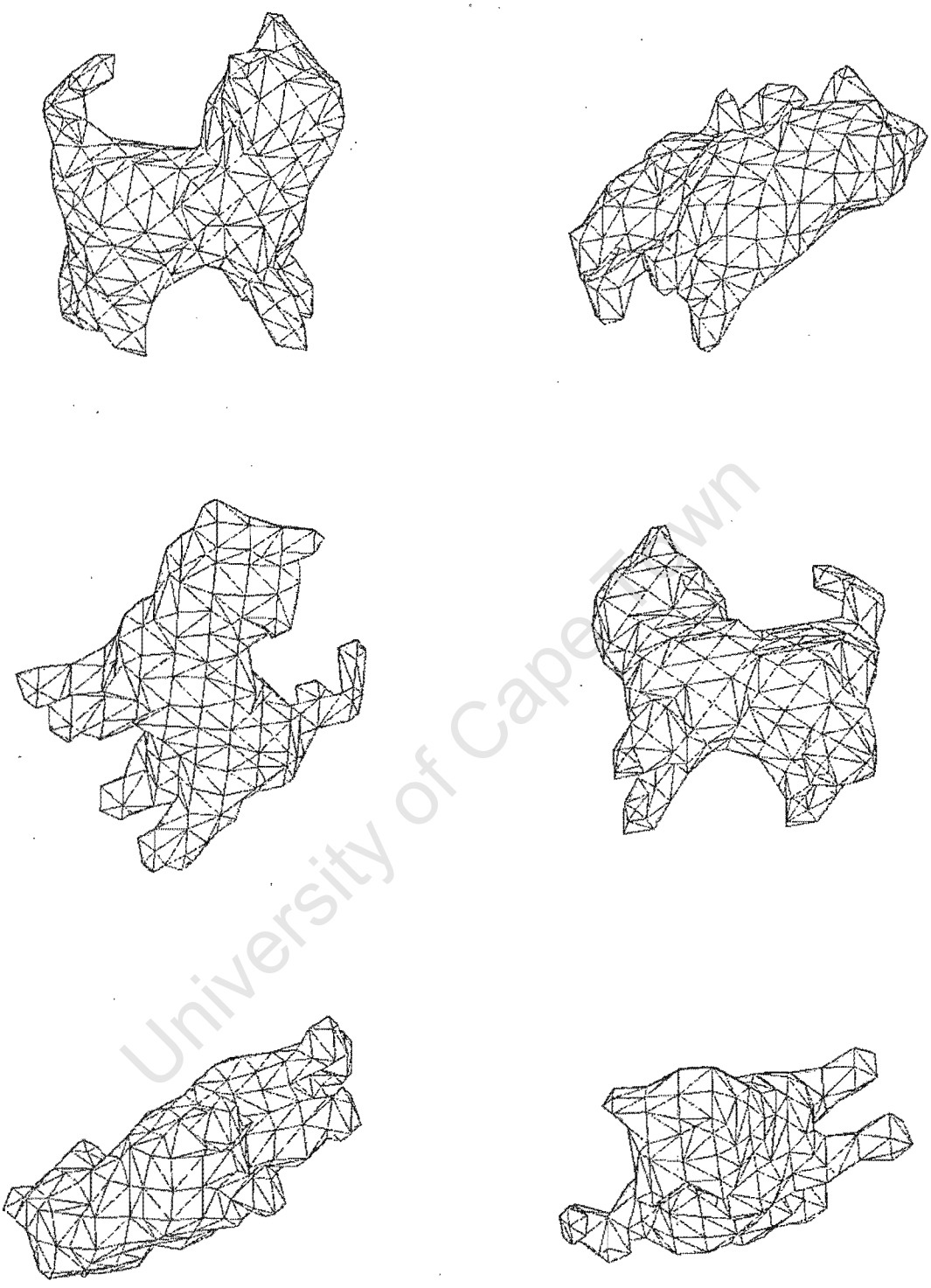

Figure 8.8: Six rotated views of the small plastic cat's visual hull, represented by marching cubes surfaces after four binary search iterations. Three subdivisions were used. Notice that high frequency detail, visible in previous images, has been removed.

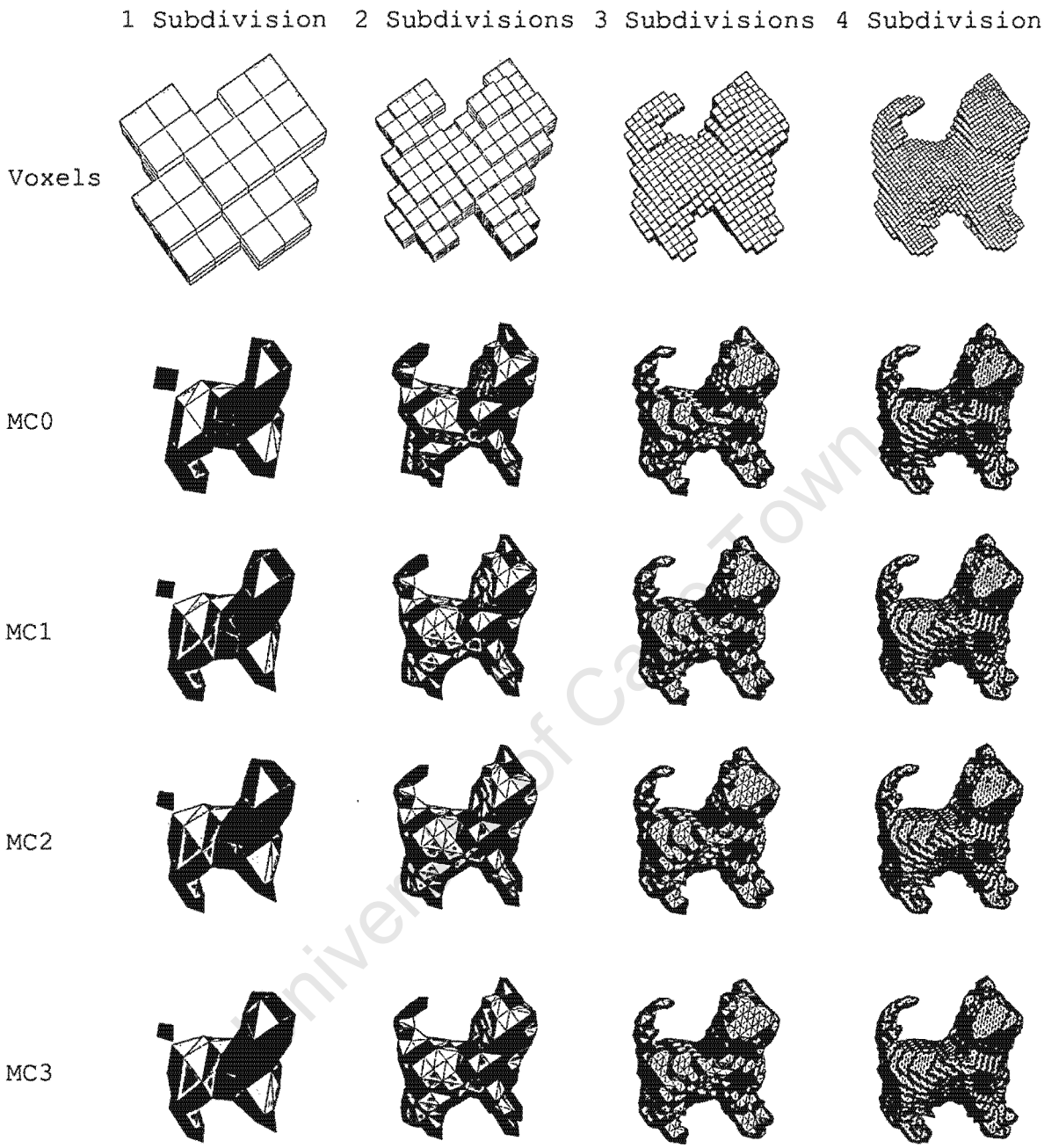

Figure 8.9: The 3D marching cubes visual hull models of the imaged cat are shown. Each column shows the visual hull at an increasing subdivision level ranging from 2 to 5. The first row shows the voxel-based visual hull models. The rows that follow, show marching cubes surfaces as more iterations of the binary search are applied. Surface colours indicate from which category in Figure A.1 the surface is from.

Chapter 9

Experimental Results

This chapter describes the results obtained from the algorithm at three different stages.

RMS and absolute mean percentage error measurements are calculated and compared. The average time used to compute each volume is also provided. Confidence intervals at 95% are made.

Abbreviations are used for each stage of the algorithm. **Voxels** is an abbreviation for "Voxel Based Visual Hull". MC-0 indicates the standard marching cubes algorithm was used and MC-1, MC-2 and MC-3 indicate the iterations of the binary search. The binary search is split into three levels so as to provide a better analysis of its performance.

9.1 Test Data Set

The stages of the algorithm were tested on a data set of 203 stones. The data set was selected so that it represented a wide distribution of shapes that occur naturally. The average dimensions of each stone was approximately $4mm \times 4mm \times 4mm = 64mm^3$. Each stone was put through a six camera system six times and the average volume was used as the computed volume ((V_m). All computations were done offline. Ground truth volumes (V_{gt}) for the entire batch of stones were calculated using Archimedes' Principal:

> *A body wholly or partially immersed in a fluid will be buoyed up by a force equal to the weight of the fluid that the body displaces.*

Stones were individually weighed in air and then in water. The accuracy of this measuring system was not tested and these volumes were used as ground truth measurements. Weight

measurements were taken in $10^{-4}\times$ grams, while volumes were measured in cubic millimetres. Using equation 9.1, the volume of each stone was computed.

$$V_{gt} = 10^3 \times \frac{W_{air} - W_{water}}{10^4}(mm^3) \tag{9.1}$$

9.2 Error Comparisons

Percentage error values are tabulated in table 9.1 and 9.2. Volume errors tend to be biased toward larger stones that produce larger errors, while percentage errors remain unaffected. Percentage errors were calculate using

$$\%E = \frac{V - V_{gt}}{V_{gt}} \times 100\% \tag{9.2}$$

RMS percentage errors were calculated using

$$\%E_{RMS} = \sqrt{\frac{\sum_{i=1}^{N}\left(\frac{V_i - V_{gt_i}}{V_{gt_i}}\right)^2}{N}} \times 100\% \tag{9.3}$$

where N is the sample size. Absolute mean errors were calculated using equation 9.4.

$$\%E_{AVG} = \frac{\sum_{i=1}^{N}\left|\frac{V_i - V_{gt_i}}{V_{gt_i}}\right|}{N} \times 100\% \tag{9.4}$$

The visual hull is usually an over estimates of an object's volume. Due to this characteristic, the computed visual hull values (V_m) are biased. To compensate for this, the values calculated are scaled by an average ratio (r) of ground truth values to measured values, to produce an estimated volume (V_{est}). It is shown that the estimated volumes are a better approximation to the actual volumes.

$$r = \frac{V_{gt}}{V_m} \tag{9.5a}$$

$$V_{est} = V_m \times r \tag{9.5b}$$

Tables 9.1 and 9.2 provide RMS and absolute mean error percentages for the measured volumes (V_m), while tables 9.3 and 9.4 provide the same errors for the estimated volume (V_{est}). In each table, columns represent the stage of the algorithm and rows represent the subdivision levels. The errors obtained using (V_{est}) are far better than those obtained using (V_m).

Res	Voxels	MC-0	MC-1	MC-2	MC-3
1	518.2%	86.3%	79.3%	78.0%	77.3%
2	277.4%	26.8%	25.7%	25.2%	25.1%
3	120.1%	7.7%	7.3%	7.2%	7.2%
4	60.2%	9.4%	9.4%	9.4%	9.4%
5	33.8%	9.9%	9.9%	9.9%	9.9%

Table 9.1: Comparison of the different percentage RMS errors calculated directly from the computed visual hull volumes (V_m).

Res	Voxels	MC-0	MC-1	MC-2	MC-3
1	463.2%	85.7%	78.8%	77.7%	77.0%
2	268.7%	16.1%	16.3%	16.3%	16.5%
3	116.9%	5.7%	5.4%	5.4%	5.3%
4	58.3%	7.4%	7.3%	7.3%	7.3%
5	32.3%	8.1%	8.1%	8.1%	8.1%

Table 9.2: Comparison of the different percentage absolute mean errors calculated directly from the computed visual hull volumes (V_m).

Res	Voxels	MC-0	MC-1	MC-2	MC-3
1	41.3%	74.9%	39.2%	32.6%	30.4%
2	18.7%	27.3%	25.1%	24.4%	24.1%
3	12.7%	7.6%	7.2%	7.1%	7.1%
4	9.5%	7.2%	7.2%	7.2%	7.3%
5	7.8%	6.6%	6.6%	6.6%	6.6%

Table 9.3: Comparison of the different % RMS errors computed using the estimated volumes (V_{est}).

As expected, with an increase in resolution, the accuracy improves. Applying marching cubes to a voxel-based model reduces the volume approximation error associated with voxel model. As the subdivision levels increase, the improvements become less pronounced (see table 9.5).

Voxels at a subdivision level of between 4 and 5 were calculated to be roughly the size of a single pixel, showing that at subdivision levels larger than 5, the accuracy of the visual hull is

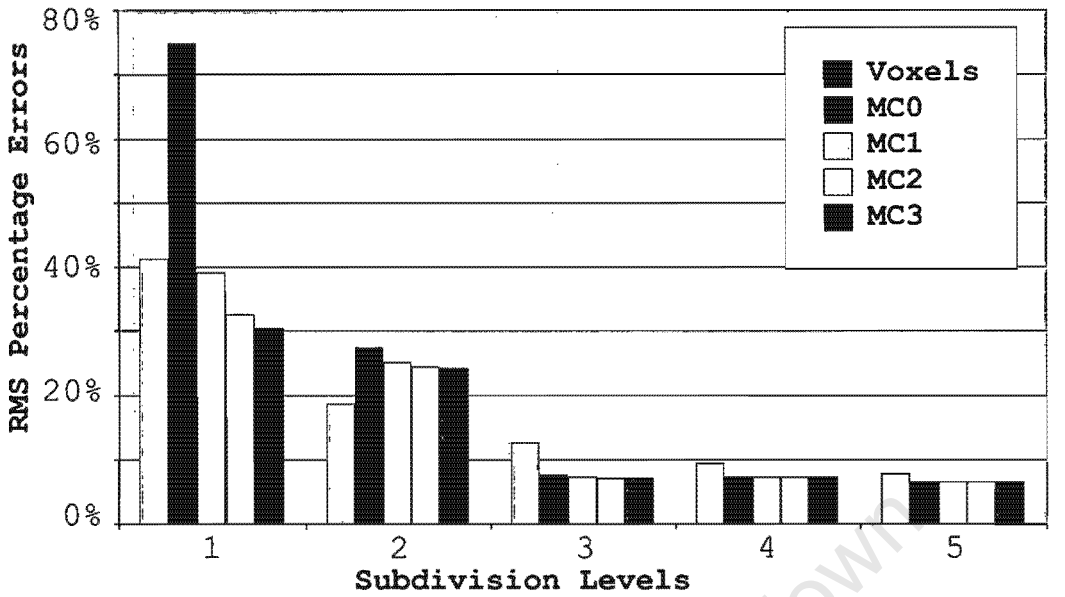

Figure 9.1: Graph of RMS percentage Errors for V_{est}.

Res	Voxels	MC-0	MC-1	MC-2	MC-3
1	30.1%	47.1%	26.9%	21.9%	20.4%
2	14.5%	15.1%	12.2%	11.6%	11.4%
3	10.0%	5.6%	5.3%	5.3%	5.3%
4	7.6%	5.3%	5.3%	5.3%	5.3%
5	6.3%	5.2%	5.2%	5.2%	5.2%

Table 9.4: Comparison of the different % absolute errors computed using the estimated volumes (V_{est}).

Res	Voxels	MC-0	MC-1	MC-2	MC-3
1 : 2	22.66%	47.58%	14.05%	8.24%	6.31%
2 : 3	5.99%	19.76%	17.96%	17.26%	17.04%
3 : 4	3.24%	0.40%	-0.04%	-0.15%	-0.20%
4 : 5	1.70%	0.58%	0.61%	0.63%	0.64%

Table 9.5: Comparison of the decrease in % RMS errors for V_{est} with an increase in resolution.

not improved. This is noticeable in the tables that follow where, between these two resolutions, minimal improvements are made.

The marching cubes have a pronounced effect on the voxel-based visual hull at all subdivision levels. Table 9.6 shows the effects that each section of the algorithm has on the accuracy of the visual hull output. The binary search on the triangle vertices also has a larger effect on the models with a lower subdivision level. At the higher levels, improvements are almost negligible. This is due to surface voxels being roughly the same size as pixels, and the binary search movements being extremely small. At higher voxel subdivision levels, the binary search has little effect on the accuracy due to surface patch movements being less than a pixel. At lower subdivision levels, the surface patches require a higher number of iterations to converge on the optimum.

Res	Voxels to MC-0	MC-0 to MC-1	MC-1 to MC-2	MC-2 to MC-3
1	-33.56%	35.72%	6.60%	2.20%
2	-8.64%	2.19%	0.79%	0.26%
3	5.12%	0.40%	0.09%	0.04%
4	2.27%	-0.04%	-0.02%	-0.01%
5	1.16%	-0.01%	0.00%	0.00%

Table 9.6: Comparison of the decrease in % RMS errors for V_{est} between the different stages of visual hull generation.

9.2.1 Confidence Intervals

In order to find a measure of how valid the error percentages are, an interval of values that have a 95% probability of containing the true mean of RMS percentage errors is computed. Intervals were calculated using the Student's t-statistic combined with the method of batch means, which applies the central limit theorem [15].

The confidence interval assumes a normally distributed population of samples. Since the population of squared percentage errors consists of only positive near zero values, the method of batch means is applied, resulting in a near normal distribution of means. The central limit theorem implies that the sample mean is approximately Gaussian. The population was split into seven batches of 29 ($7 \times 29 = 203$). The mean of each batch was computed and these values were used in equation 9.6. Batch means were used to compute the confidence interval as the mean of batch means in equal to the mean of the total population. Squared percentage errors were obtained from estimated volume measurements (V_{est}).

Equation 9.6 provides the formula for a $(1-\alpha)100\%$ confidence interval. To obtain a 95% confidence interval, $\alpha = 0.05$. The t-statistic ($t_{\alpha/2}$) can be found in a lookup table or by using MATLAB's `TINV` function.

$$\overline{S_{\%E^2}} - t_{\alpha/2}\frac{s_{\%E^2}}{\sqrt{N}} < \mu_{\%E^2} < \overline{S_{\%E^2}} + t_{\alpha/2}\frac{s_{\%E^2}}{\sqrt{N}} \tag{9.6}$$

$\overline{S_{\%E^2}}$ is the sample mean of squared percentage errors, $s_{\%E^2}$ is the sample standard deviation of squared percentage errors, $\mu_{\%E^2}$ is the true population mean of squared percentage errors, and N is the batch size.

The square root of the above values gives the RMS percentage errors. RMS confidence intervals at 95% for each method using the estimated volumes (V_{est}) are shown in tables 9.7, 9.8, 9.9, 9.10 and 9.11. The size of an interval is indicated in the last column of each table ($|Interval|$). A plot for each table is also provided.

Method	Resolution of 1 at 95%	$\|Interval\|$
Voxel	$36.9\% < \%Error_{RMS} < 45.4\%$	8.5%
MC-0	$63.9\% < \%Error_{RMS} < 84.5\%$	20.7%
MC-1	$35.7\% < \%Error_{RMS} < 42.4\%$	6.7%
MC-2	$30.7\% < \%Error_{RMS} < 34.4\%$	3.7%
MC-3	$26.2\% < \%Error_{RMS} < 34.1\%$	8.0%

Table 9.7: The 95% confidence intervals of V_{est} % RMS errors with the resolution at 1 subdivision level.

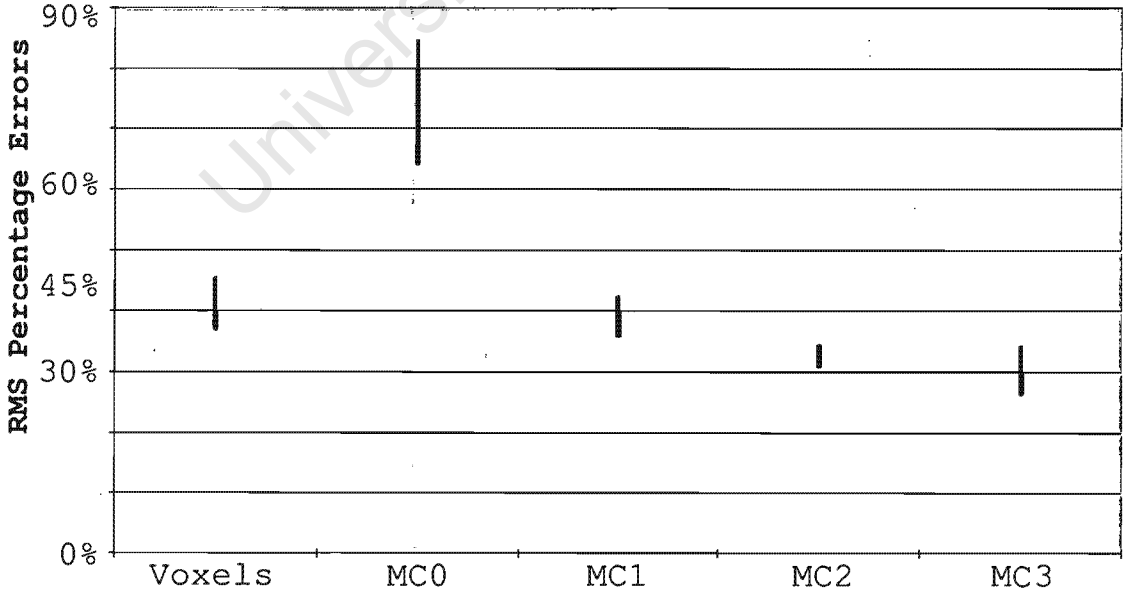

Figure 9.2: Graph of 95% Confidence Intervals for Resolution 1.

Method	Resolution of 2 at 95%	$\|Interval\|$
Voxel	$17.0\% < \%Error_{RMS} < 20.2\%$	3.2%
MC-0	$7.7\% < \%Error_{RMS} < 37.9\%$	30.2%
MC-1	$9.4\% < \%Error_{RMS} < 34.3\%$	24.9%
MC-2	$12.5\% < \%Error_{RMS} < 32.1\%$	19.6%
MC-3	$12.0\% < \%Error_{RMS} < 31.9\%$	19.8%

Table 9.8: The 95% confidence intervals of V_{est} % RMS errors with the resolution at 1 subdivision levels.

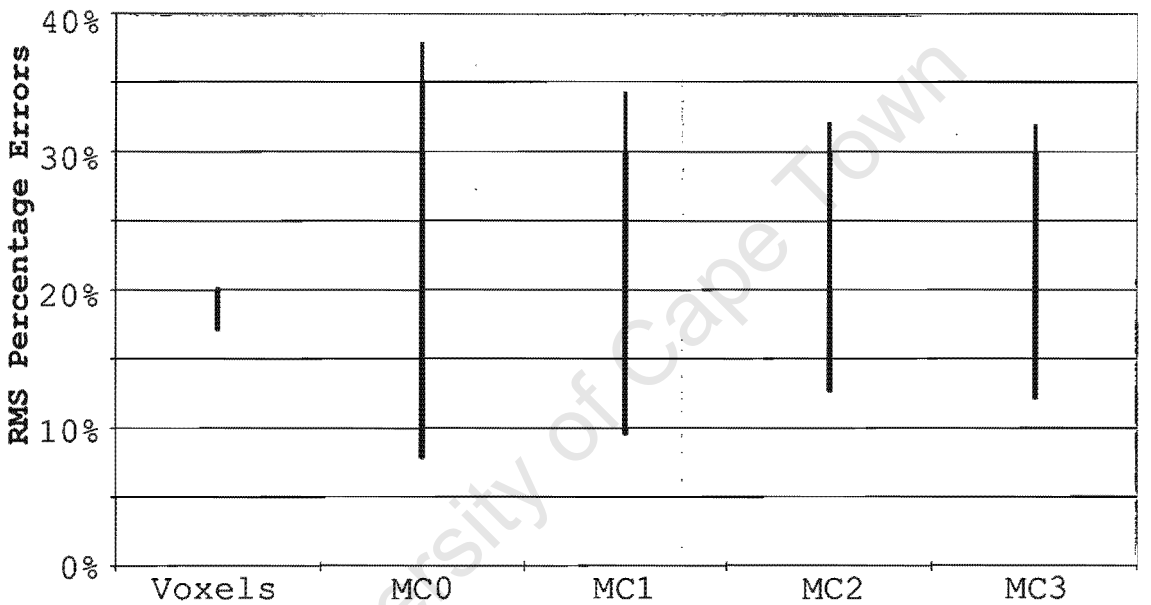

Figure 9.3: Graph of 95% Confidence Intervals for Resolution 2.

Method	Resolution of 3 at 95%	$\|Interval\|$
Voxel	$11.5\% < \%Error_{RMS} < 13.8\%$	2.2%
MC-0	$6.7\% < \%Error_{RMS} < 8.3\%$	1.6%
MC-1	$6.5\% < \%Error_{RMS} < 7.8\%$	1.3%
MC-2	$6.3\% < \%Error_{RMS} < 7.8\%$	1.6%
MC-3	$6.0\% < \%Error_{RMS} < 8.0\%$	2.0%

Table 9.9: The 95% confidence intervals of V_{est} % RMS errors with the resolution at 1 subdivision levels.

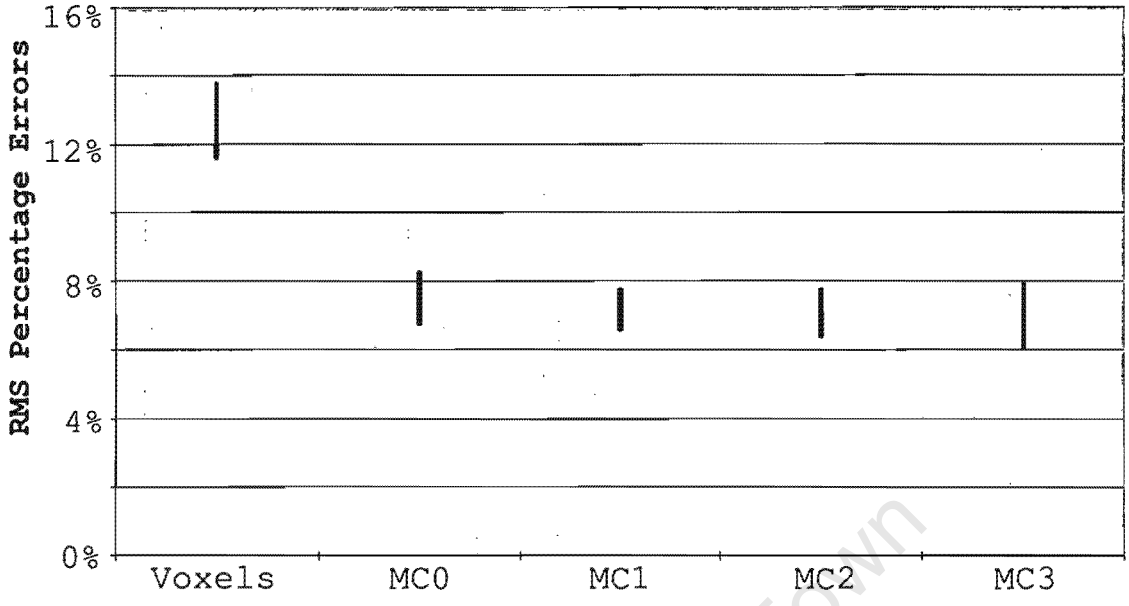

Figure 9.4: Graph of 95% Confidence Intervals for Resolution 3.

Method	Resolution of 4 at 95%	$\|Interval\|$
Voxel	$8.7\% < \%Error_{RMS} < 10.1\%$	1.4%
MC-0	$6.3\% < \%Error_{RMS} < 8.0\%$	1.7%
MC-1	$6.3\% < \%Error_{RMS} < 8.0\%$	1.7%
MC-2	$6.8\% < \%Error_{RMS} < 7.7\%$	0.9%
MC-3	$6.4\% < \%Error_{RMS} < 8.0\%$	1.6%

Table 9.10: The 95% confidence intervals of V_{est} % RMS errors with the resolution at 1 subdivision levels.

Method	Resolution of 5 at 95%	$\|Interval\|$
Voxel	$6.8\% < \%Error_{RMS} < 8.6\%$	1.8%
MC-0	$5.9\% < \%Error_{RMS} < 7.3\%$	1.4%
MC-1	$6.1\% < \%Error_{RMS} < 7.1\%$	1.0%
MC-2	$6.1\% < \%Error_{RMS} < 7.1\%$	1.0%
MC-3	$6.1\% < \%Error_{RMS} < 7.1\%$	1.0%

Table 9.11: The 95% confidence intervals of V_{est} % RMS errors with the resolution at 1 subdivision levels.

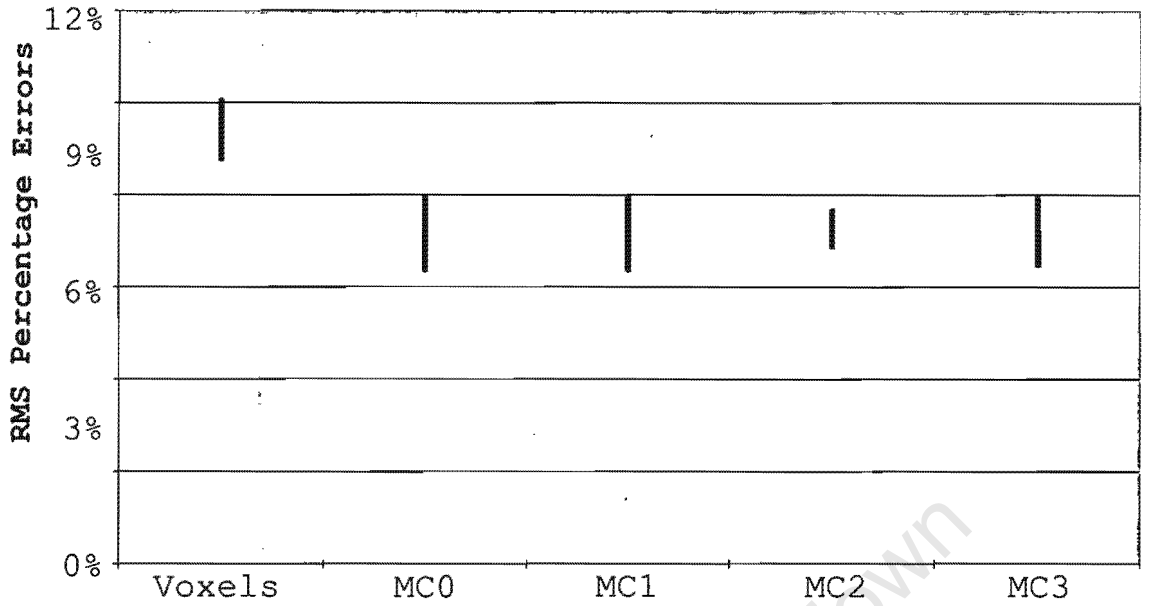

Figure 9.5: Graph of 95% Confidence Intervals for Resolution 4.

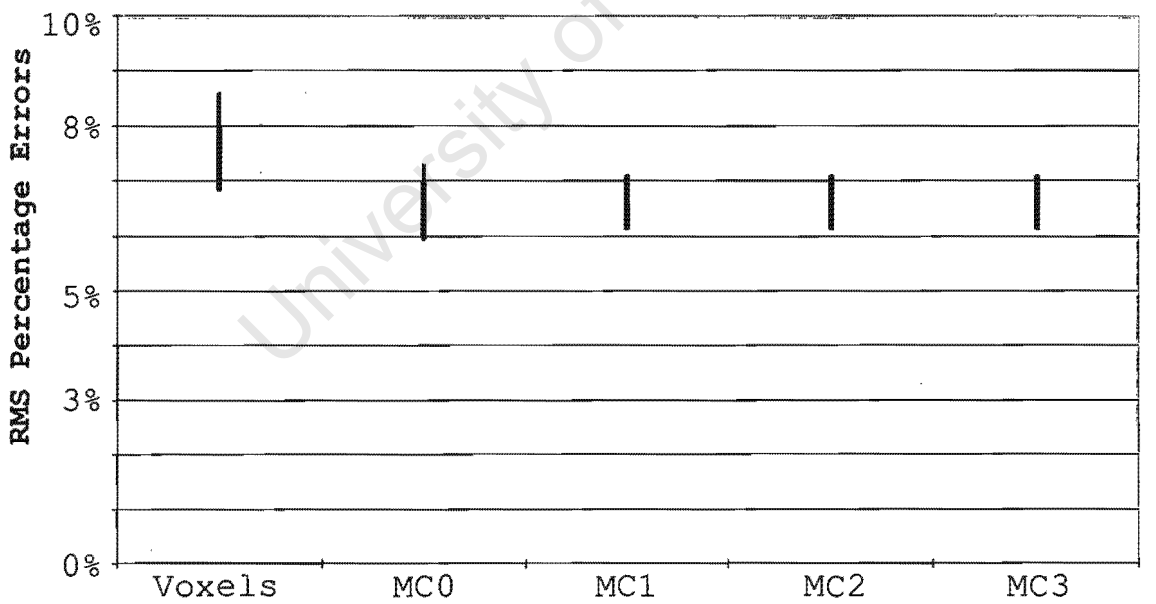

Figure 9.6: Graph of 95% Confidence Intervals for Resolution 5.

The confidence interval tables and their associated graphs show that at a higher subdivision level, we can be generally more confident that the errors are low. At the highest level (see table 9.11),

the binary search has minimal effect. This is also slightly evident at a subdivision level of 4 (see table 9.10).

9.3 Time Comparisons

Table 9.12 contains the average time in seconds required to compute the visual hull for each method at various subdivision levels.

Res	Voxels	MC-0	MC-1	MC-2	MC-3
1	0.077s	0.050s	0.052s	0.053s	0.055s
2	0.330s	0.263s	0.277s	0.291s	0.305s
3	1.905s	1.894s	1.956s	2.015s	2.075s
4	14.380s	14.712s	14.966s	15.215s	15.461s
5	114.037s	116.408s	117.458s	118.468s	119.500s

Table 9.12: Speed comparisons for voxels, marching cubes and binary searches. Rows represent the hull models at increasing subdivision levels. Columns represent the different methods used.

From this data, tables 9.14, 9.15 and 9.13 were generated. Using table 9.14, it is clear that the voxel generation takes up the majority of the time, and by applying marching cubes, the average difference in time is roughly 10%. The decrease in speed between voxels and marching cubes at lower subdivision levels is due to the marching cubes algorithm using a smaller output structure. Table 9.15 shows that the various iterations of the binary search have minimal effect on the running time of the algorithm.

As expected, table 9.13 shows that a single increment in subdivision level requires roughly six times more processing time. This increase in time is shown to be relatively consistent throughout.

9.4 Number of Elements

Table 9.16 shows how, as the subdivision level increases, the ratio of voxel elements to surface patches decreases. This means that the marching cubes algorithm uses less elements than voxel-based methods as the resolution increases.

At lower subdivision levels, a voxel-based model requires fewer voxel elements to build the visual hull than marching cubes requires surfaces. As the level increases, the ratio decreases.

Res	Voxels	MC-0	MC-1	MC-2	MC-3	Avg
1 : 2	330%	423%	431%	444%	454%	417%
2 : 3	477%	619%	607%	593%	581%	576%
3 : 4	655%	677%	665%	655%	645%	659%
4 : 5	693%	691%	685%	679%	673%	684%
Avg	539%	602%	597%	593%	588%	584%

Table 9.13: This table shows the effect that an increase in subdivision level has on the computational time. Rows represent the percentage increase in processing time required to compute the visual hull. Columns represent the different methods used.

Res	Voxel to MC
1	-34%
2	-20%
3	-1%
4	2%
5	2%
Avg	-10%

Table 9.14: This table shows the percentage increase in time required when applying the marching cubes algorithm to a voxel-based visual hull model.

Res	MC-0 to MC-1	MC-1 to MC-2	MC-2 to MC-3	Avg
1	3%	3%	3%	3%
2	5%	5%	5%	5%
3	3%	3%	3%	3%
4	2%	2%	2%	2%
5	1%	1%	1%	1%
Avg	2.828%	2.649%	2.642%	2.706%

Table 9.15: This table shows the effect that the various iterations of the binary search have on the time required to compute the visual hull.

This is due to the voxel model having a high number of interior voxels which have no surface passing through them. In a visual hull model, the relationship between the ratio of voxels to surface patches is affected by the relationship between the objects surface area and it volume. An object with a large surface area relative to a low volume will have less triangular patches in its surface than voxel elements (e.g. a cat). The opposite is true of an object with a small surface area relative to a large volume (e.g. a sphere).

Res	Voxels	MC
1	9	9
2	48	86
3	228	363
4	1348	1509
5	9078	6233

Table 9.16: The average number of elements for voxels vs marching cubes at various subdivision levels.

Chapter 10

Conclusions

A system is presented that allows for the fast computation of an object's visual hull from multiple view silhouette images. The algorithm is analysed at three key stages:

- Voxelisation of a volume that contains the target.
- Approximation of the surface passing through exterior voxels.
- Positional accuracy of the surface is improved with a binary search.

As can be seen in the results, a high resolution voxel-based visual hull is computationally very expensive when compared to the visual hull produced by the marching cubes algorithm at a similar accuracy percentage. It was also found that the binary search has a negligible effect on the amount of time required.

The visual hull model, computed with the marching cubes algorithm, using a voxel subdivision level of 3 and a binary search with 3 iterations, has an RMS error with a 95% chance of being between 6% and 8%. This visual hull took, on average, 1.78% of the time to compute as the voxel-based model with an equivalent error. Visual hull models with 5 subdivision levels and binary search iterations of 2 and 3 produce the most accurate results, but require the largest amount of time to compute.

An advantage of the marching cubes algorithm is that the visual hull it represents is computationally easier to manipulate than a voxel-based visual hull. The binary search improves the positional accuracy of each vertex and hence gives a better approximation to the actual surface that passes through the voxel. Its effects are less noticeable at higher subdivision levels.

10.1 Limitations

Representing an object's visual hull with a number of voxels is a simple concept, and easily implemented. The large number of voxels used to make up the visual hull can cause other systems using these models to become sluggish. When rendering a voxel-based model, only surface voxels are visible. Internal voxels are useful when computing the centroid or volume of a model, but are otherwise redundant.

The marching cubes algorithm requires all voxels to be the same size, resulting in the octree structure losing its advantage of compression. The octree structure provides no consistent notion of object connectivity, which means that each voxel is tested as a completely separate entity causing a large number of shared vertices to be repetitively tested. Another limitation of this data structure is that, if a minimum subdivision level is specified, parts of the object can be omitted and cause inconsistencies. The marching cubes sections of the algorithm inherit the inconsistencies and can produce unreliable results. The same problems occur due to assumptions made about a voxel's occupancy category. Objects with snake-like extrusions or with sharp peaks can appear discontinuous at lower resolutions (see Figure 5.4).

As in the standard MC15 algorithm, this algorithm's computational expenses can be reduced by minimising the number of triangles contained in lookup table surfaces. The use of polygons in place of triangles is also an option.

10.2 Website Tutorial

A MATLAB tutorial can be downloaded from the author's website:
`http://dsp7.ee.uct.ac.za/~phillip`

The tutorial uses MEX wrappers to implement C++ code. Sample data of the small plastic cat is provided. The C++ code used to implement the voxel-based visual hull as well as the code for the marching cubes algorithm at varying subdivision levels is also available.

10.3 Scope for Further Investigation

Speed improvements for computing a voxel model can be achieved by excluding already computed shared vertices. Including some notion of voxel connectivity makes this feasible.

Texture mapping sections of the imaged object onto the visual hull would improve the visual effects of the output, making it more pleasing to the eye. This can be done by projecting a surface patch into the camera image with the best view of the patch. All pixel values inside the boundary of the patch are then used as texture for the patch. The best camera view can be determined by projecting the patch normal and finding the minimum angle between the projected normal and each camera's optical axis.

Appendix A

Chernyaev's MC33 Marching Cube Surfaces

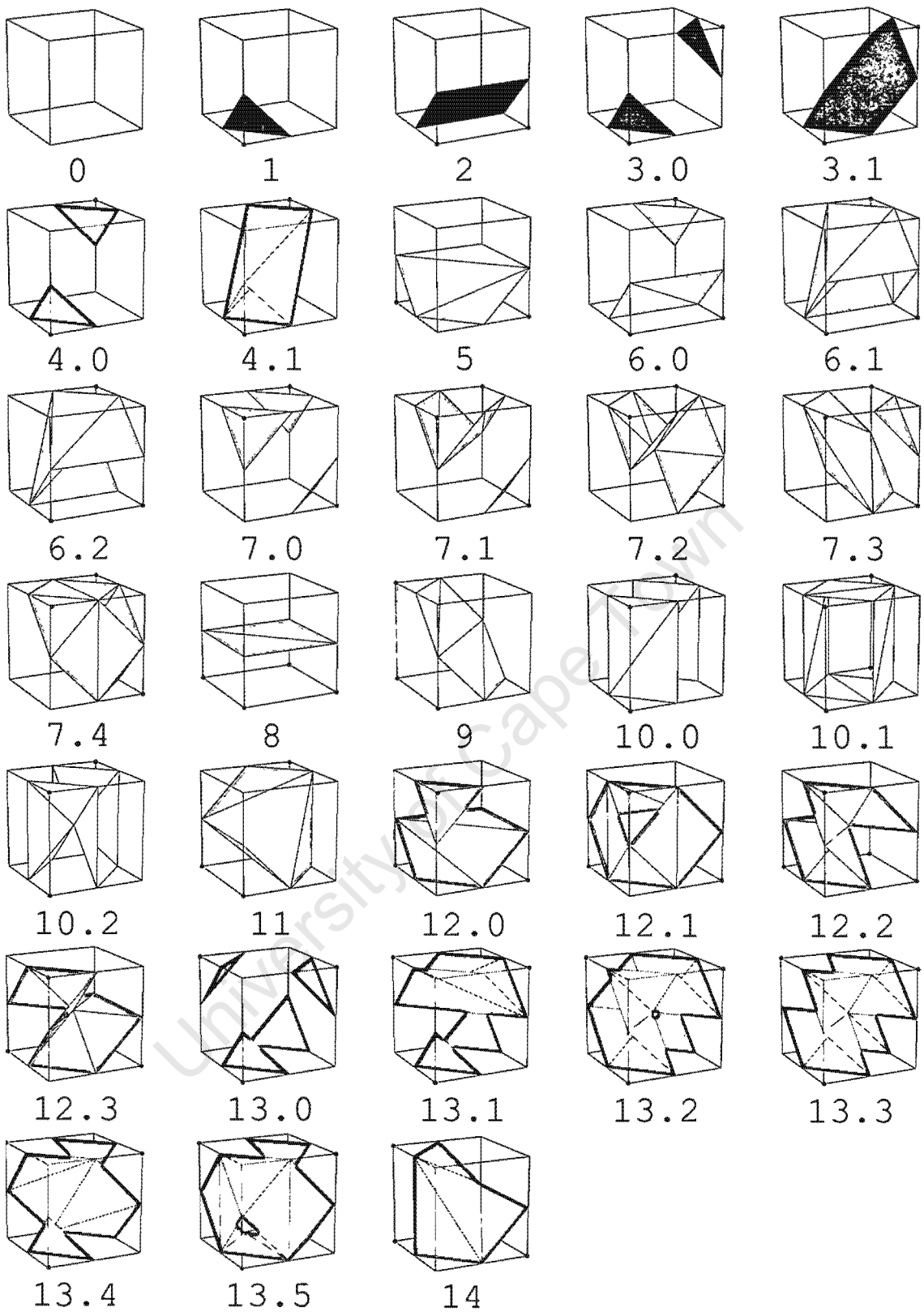

Figure A.1: Chernyaev's 33 marching cube surfaces[16].

Appendix B

Lookup Table for the MC33 Cube Categories

Case	Face Test			Interior Test	Sub-Case	No. of Triangles
	1st	**2nd**	**3rd**			
0						0
1						1
2						2
3	-				3.1	2
	+				3.2	4
4	-				4.1	2
	+				4.2	6
5						3
6	-			-	6.1.1	3
	-			+	6.1.2	7
	+				6.2	5
7	-	-	-		7.1	3
	+	-	-		7.2	5
	-	+	-		7.2	5
	-	-	+		7.2	5
	+	+	-		7.3	9
	+	-	+		7.3	9
	-	+	+		7.3	9
	+	+	+	+	7.4.1	9
	+	+	+	-	7.4.2	9
8						2
9						4
10	+	+			10.1.1	4
	-	-		-	10.1.1	4
	-	-		+	10.1.2	8
	+	-			10.2	8
	-	+			10.2	8
11						4
12	+	+			12.1.1	4
	-	-		-	12.1.1	4
	-	-		+	12.1.2	8
	+	-			12.2	8
	-	+			12.2	8
13	45 subcases, testing all the 6 faces and eventually the interior.					
14						4

Table B.1: A reduced representation of the test table. Case 13 has 45 entries to map the results of all the possible tests to the right subcase[23].

Bibliography

[1] Narendra Ahuja and Jack Veenstra. Generating octrees from object silhouettes in orthographic views. *IEEE Transactions on Pattern Analysis and Machine Intelligence*, 11(2):137–149, February 1989.

[2] Mark D. Anderson. Delineation of the left ventricle using snakes. The University of Cape Town, October 2001. Bachelor's Thesis.

[3] B.G. Baumgart. *Geometric Modelling for Computer Vision.* PhD thesis, Stanford University, 1974.

[4] Ricardo Chavarriaga and Raquel Urtasun. Camera calibration. Technical report, Graduate School in Computer Science, Switzerland, January 2001.

[5] Evgeni V. Chernyaev. Marching cubes 33: Construction of topologically correct isosurfaces. Technical report, 1995. CERN CN 95-17, CERN.

[6] Kong Man Cheung. *Visual Hull Construction, Alignment and Refinement for Human Kinetic Modelling, Motion Tracking and Rendering.* PhD thesis, Carnegie Mellon University, June 2003.

[7] Oliver Faugeras and Quang-Tuan Luong. *The Geometry of Multiple Images.* The MIT Press, 2001.

[8] Keith Forbes, Anthon Voigt, and Ndimi Bodika. An inexpensive, automatic and accurate camera calibration method. In *Proceedings of the Thirteenth Annual South African Workshop on Pattern Recognition*, pages 1–6. PRASA, November 2002. ISBN 0-7992-2147-3.

[9] David A. Forsyth and Jean Ponce. *Computer Vision - A Modern Approach.* Prentice Hall, 2003.

[10] M.G. Hamblin and G.W. Stachowiak. Variation of particle shape parameters when viewed as a projection and a section. *Journal of Computer-Assisted Microscopy*, 6(2):51–59, 1994.

[11] F. Lanaro and P. Tolppanen. 3D characterization of coarse aggregates. *Engineering Geology 65*, 2001.

[12] John Zaniewskic Larry Bantaa, Ken Chengb. Estimation of limestone particle mass from 2D images. Technical report, Powder Technology, November 2002.

[13] Aldo Laurentini. The visual hull: A new tool for contour-based image understanding. In *7th Scandinavian Conference on Image Analysis*, pages 993–1002, 1991.

[14] Aldo Laurentini. The visual hull concept for silhouette-based image understanding. In *IEEE Transactions on Pattern Analysis and Machine Intelligence*, volume 16, pages 150–162, February 1994. Also available at http://www.polito.it/bottino/Articles/pami94.pdf.

[15] Alberto Leon-Garcia. *Probability and Random Processes for Electrical Engineering*. Adison-Wesley Publishing Company, 2nd edition, May 1994. ISBN 0-201-50037-X.

[16] Thomas Lewiner, Hlio Lopes, Antnio Wilson Vieira, and Geovan Tavares. Efficient implementation of marching cubes cases with topological guarantees. *Journal of Graphics Tools*, 8(2):1–15, 2003.

[17] Sheue ling Lien and James T. Kajiya. A symbolic method for calculating the integral properties of arbitrary nonconvex polyhedra. *IEEE Computer Graphics and Applications*, 4(10):35–41, October 1984.

[18] William E. Lorensen and Harvey E. Cline. Computer graphics. *Marching Cubes: A High Resolution 3D Surface Reconstruction*, 21(4):163–166, July 1987.

[19] Chien-Ping Lu, Gregory D. Hager, and Eric Mjolsness. Fast and globally convergent pose estimation from video images. *IEEE Transactions on Pattern Analysis and Machine Intelligence*, 22(6):610–622, June 2000.

[20] W. N. Martin and J. K. Aggarwal. Volumetric descriptions of objects from multiple views. In *IEEE Transactions on Pattern Analysis and Machine Intelligence*, volume 5, pages 150–158, March 1983.

[21] Wojciech Matusik, Chris Buehler, and Leonard McMillan. Polyhedral visual hulls for real-time rendering. In *Proceedings of Twelfth Eurographics Workshop on Rendering*, pages 115–125, June 2001.

[22] Phillip Milne. Pixel based segmentation using region growing techniques. The University of Cape Town, December 2001. Bachelor's Thesis.

[23] C. Montani, R. Scateni, and R. Scopigno. Discretized marching cubes. In R. D. Bergeron and A. E. Kaufman, editors, *Visualization '94 Proceedings*, pages 281–287, Washington D. C., USA, 1994. IEEE Computer Society, IEEE Computer Society Press. citeseer.ist.psu.edu/montani94discretized.html.

[24] Gregory. M. Nielson and Bernd. Hamann. The asymptotic decider: Resolving the ambiguity in marching cubes. In *Proceedings of Visualization '91*, pages 29–38, October 1991.

[25] W. Niem and R. Buschmann. Automatic modelling of 3D natural objects from multiple views. In European Workshop on Combined Real and Synthetic Image, November 1994. Hamburg, Germany.

[26] Karin Olsson and Therese Persson. Shape from silhouette scanner. Master's thesis, University of Linkoping, Sweden, 2001.

[27] Marc Pollefeys. *Tutorial on 3D Modelling from Images*, June 2000. In conjunction with ECCV 2000.

[28] Chetana Rao, Erol Tutumluer, and Joseph A. Stefanski. Coarse aggregate shape and size properties using a new image analyzer. *ASTM Journal of Testing and Evaluation*, November 2000.

[29] G. Shakhnarovich, L. Lee, and T. Darrell. Integrated face and gait recognition from multiple views. In *IEEE Computer Society Conference on Computer Vision and Pattern Recognition*, 2001.

[30] Daniel E. Small. Real time shape from silhouette. Master's thesis, The University of New Mexico, July 2001.

[31] M. Tarini, M. Callieri, C. Montani, C. Rocchini, K. Olsson, and T. Persson. Marching intersections: An efficient approach to shape-from-silhouette. In *7th International Fall Workshop on Vision, Modeling, and Visualization*, November 2002.

[32] Emanuele Trucco and Alessandro Verri. *Introductory Techniques for 3D Computer Vision*. Prentice Hall PTR, 1998. ISBN 0132611082.

[33] R. Y. Tsai. A versatile camera calibration technique for high-accuracy 3D machine vision metrology using off-the-shelf TV cameras and lenses. *IEEE Journal of Robotics and Automation*, RA-3(4):232–344, August 1987.

[34] Kwan-Yee Kenneth Wong. *Structure and Motion from Silhouettes*. PhD thesis, University of Cambridge, 2001.